

Casalino, M., Coppola, G., De La Rue, R. M., and Logan, D. F. (2016) State-of-the-art all-silicon sub-bandgap photodetectors at telecom and datacom wavelengths. *Laser and Photonics Reviews*, 10(6), pp. 895-921.

There may be differences between this version and the published version. You are advised to consult the publisher's version if you wish to cite from it.

This is the peer reviewed version of the following article: Casalino, M., Coppola, G., De La Rue, R. M., and Logan, D. F. (2016) State-of-the-art all-silicon sub-bandgap photodetectors at telecom and datacom wavelengths. *Laser and Photonics Reviews*, 10(6), pp. 895-921, which has been published in final form at <http://dx.doi.org/10.1002/lpor.201600065>. This article may be used for non-commercial purposes in accordance with [Wiley Terms and Conditions for Self-Archiving](#).

<http://eprints.gla.ac.uk/137714/>

Deposited on: 3 March 2017

Article type: Review Article

Title: State of the art all-silicon sub-bandgap photodetectors at telecom and datacom wavelengths

Maurizio Casalino^{1,}, Giuseppe Coppola¹, Richard M. De La Rue², and Dylan F. Logan³*

*Corresponding Author: E-mail: maurizio.casalino@na.imm.cnr.it

¹Institute for Microelectronics and Microsystems of the National Research Council, Via P. Castellino n. 111, 80131, Italy

²Optoelectronics Research Group, School of Engineering, University of Glasgow, Rankine Building, Oakfield Avenue, Glasgow G12 8LT, Scotland, U.K.

³RANOVUS, 16 Fitzgerald Rd., Suite 100, Ottawa, ON, Canada

Silicon-based technologies provide an ideal platform for the monolithic integration of photonics and microelectronics. In this context, a variety of passive and active silicon photonic devices have been developed to operate at telecom and datacom wavelengths, at which silicon has minimal optical absorption - due to its bandgap of 1.12 eV. Although in principle this transparency window limits the use of silicon for optical detection above 1.1 μm , in recent years tremendous advances have been achieved in the field of all-silicon sub-bandgap photodetectors at telecom and datacom wavelengths - by taking advantage of new emerging materials and structures. In this paper, a review of the state of the art is presented. Devices based on defect-mediated absorption, two-photon absorption and the internal photoemission effect are reported, their working principles are elucidated and their performance discussed and compared.

1. Introduction

Due to recent breakthroughs, silicon (Si) photonics is now the most active discipline within the field of integrated optics and, at the same time, a present reality - with commercial

products already available on the market.[1-2] Silicon photodiodes are excellent detectors at visible wavelengths, but the development of high-performance photodetectors (PDs) on silicon CMOS platforms at wavelengths of interest for telecom and datacom applications has remained an imperative but so far unaccomplished task. By focusing on a hybrid approach over the past decades, various technological processes have been investigated to make near-infrared absorbing material compatible with CMOS technology. Among them, high performance photodetectors, based mainly on InGaAs [3-4] and Ge [5], have been demonstrated. Unfortunately, their direct integration with silicon is limited, due to the lattice mismatch, which causes a substantial level of surface roughness and a high density of threading dislocations that degrade the device performance. Indeed, although InGaAs has a nearly perfect lattice match with that of an InP substrate, allowing the fabrication of high-performance InGaAs/InP heterostructure devices, the 8.1% lattice mismatch between InP and Si makes InGaAs photodetectors difficult to integrate with CMOS circuits.[6] Ge is another competitive material for photodetection at telecom wavelengths and there has been considerable effort to establish technological processes capable of overcoming the 4.2% lattice mismatch between Ge and Si. Currently, the most commonly employed solution is to use a two-step epitaxial growth technique that complicates the CMOS fabrication flow-chart significantly and increases the cost per device.[6-7] There would therefore be a major cost-benefit provided by implementation of the monolithic integration of photodiodes (PDs) and electronics in a single silicon die, offering simplified fabrication and a useful scale-up of manufacture. While many papers and several reviews have been published on near-infrared Si PDs based on hybrid approaches (with germanium, InGaAs, etc..) [6, 8-9], very little has been published on the possibility of detecting light at sub-bandgap wavelengths in Si. In 2010 a review article was published on all-Si PDs at telecom wavelengths [10], where the authors distinguished the three main absorption mechanisms for Si sub-bandgap photo-detection

currently being investigated: the internal photoemission effect (IPE), two-photon absorption (TPA) and defect-mediated absorption – including both surface defect-mediated absorption (SDA) and bulk defect-mediated absorption (BDA).

In recent years much effort has been focused on the field of sub-bandgap all-Si PDs and both new structures and new results have been reported. In particular, the IPE-based effect has been combined with nanoscale metallic structures integrated on Si substrates, including: Si nanoparticles (NPs) [11], metal stripes supporting surface plasmon polaritons (SPPs) [12, 13], antennas [14] and metallic gratings.[15] Moreover IPE has been investigated in novel Si structures based on two-dimensional materials like graphene that can replace metal in the Schottky junction - showing very promising results.[16] In addition, very recently, the advantages of PDs based on an all-Si approach have been extended to the 2 μm wavelength region, impacting significantly on the area of optical data communication.[17] Indeed, two-photon absorption, which is a limiting factor for nonlinear optical processes in the NIR, vanishes at longer wavelengths where, moreover, the success of Ge cannot be extended, due to its cutoff wavelength.[18] Finally, it is worth noting that the efficiency and sensitivity of PDs based on the aforementioned effects can be adequately enhanced by fabricating structures that support avalanche effects.[19]

The aim of the present review is both to summarize the fundamentals of sub-bandgap photo-conversion in silicon and to highlight the advances made in this field since 2010. An overview of the state of the art in sub-bandgap all-silicon photodetectors working at both telecom and datacom wavelengths is presented. Firstly, the physical effects and the working principles of these devices are elucidated, then the main structures reported in the literature and the most significant results obtained in recent years are reviewed and discussed, comparing the performance of devices based on the different approaches. Finally, the potential of all-silicon

sub-bandgap PDs, which take advantage of both newly emerging materials and smart structures, will be addressed.

2. Performance specifications

To provide quantitative comparisons between photo-detectors, certain figures of merit need to be defined. High quantum-efficiency, high bandwidth, low dark-current, low bias-voltage and small dimensions are common design targets for a PD.

The quantum efficiency η is the number of carriers that can be collected per photon. It is worth noting that there is a difference between internal and external quantum efficiency: in the case of the internal quantum efficiency (η_i), the number of carriers that contribute to the photocurrent is related to the number of absorbed photons - while, in the case of the external quantum efficiency (η_e), the photocurrent is related to the number of incident photons. η_e and η_i are strictly linked by the formula $\eta_e = A \cdot \eta_i$, where A is the absorbance of the active material. A very common efficiency measure is named responsivity and represents the ratio between the measurable magnitudes: the photo-generated current and the optical power. Responsivity and quantum efficiency are strictly linked:

$$R = \frac{\lambda}{1242} \cdot \eta \quad (1)$$

where λ is the wavelength of operation in nanometres. Of course, depending on whether the responsivity is referred to the internal or to the external quantum efficiency, it is possible to speak of internal responsivity (the ratio between photo-generated current and absorbed optical power) and external responsivity (conventionally and in the present manuscript referred to as simply responsivity, i.e., the ratio between photo-generated current and incident optical power), respectively. Substantial responsivity (>0.1 A/W) is necessary for an acceptable signal-to-noise ratio - and to ease the design and realization of the amplifier circuitry that follows.

Bandwidth is another important parameter for a PD. As information bandwidth demands in telecommunications systems and optical interconnects continue to increase, it is essential that all-silicon photodetectors be able to operate at bandwidths of at least 5 GHz, a frequency at which hybrid detectors have already been demonstrated.[20] Of course, higher bandwidths (>50 GHz) are desirable, in order to anticipate future trends in optical interconnects. In fact, very high-speed photodetectors, combined with dense wavelength division multiplexing (DWDM) technology in the *C* band (1528–1561 nm) and *L* band (1561–1620 nm) [21], have the potential to achieve an information bandwidth greater than 0.5 THz.

An important property in the evaluation of PD signal quality is dark current, which is the amount of the output current that is independent of the incident optical power level. Dark currents less than 1 μA are typically required. Dark current is a serious issue because it is responsible for increases in both the noise equivalent power (NEP, i.e., the minimum detectable optical power) and the bit error rate (BER). BER is really critical in datacom systems where the consequences of even a single bit error can be very serious. Indeed, typical telecom systems operate at a BER of about 10^{-9} , compared with about 10^{-12} to 10^{-15} for datacom systems [22].

A further requirement of the PDs is low-voltage operation. It is desirable to realize devices that operate at the same power supply voltage as the CMOS circuitry, i.e., bias voltage < 5 V and as low as 1 V for advanced generations of CMOS.

Finally, the shrinking of photodetector dimensions will allow for easier integration of photonic components with integrated electronic circuits, enabling interconnection bandwidths that are not limited by the RC time constants or the reliability constraints of metal connection lines.

3. Silicon sub-bandgap photo-detection mechanisms

In this section the physical effects responsible for the sub-bandgap photo-detection in Si are elucidated and discussed in detail.

3.1. Internal photoemission effects (IPE)

The internal photoemission effect (IPE) is the optical excitation of electrons in the metal to energy levels above the Schottky barrier and then the transport of these electrons to the energy bands of the semiconductor - as shown in Figure 1, where p-type Si is considered.

The original electron photoemission model from metal into vacuum was described by Fowler.[23] In the 1960s, Fowler's model was modified - in order to make it suitable for description of the carrier photoemission from metal into a semiconductor by Cohen, Vims and Archer [24], producing the very commonly used formula:

$$\eta_i = C \cdot \frac{(h\nu - \phi_B)^2}{h\nu} \quad (2)$$

where $h\nu$ is the energy photon, ϕ_B is the Schottky barrier, $C=1/8(E_F+\phi_B)$ is called the quantum efficiency coefficient and E_F is the Fermi level of the metal. Equation 2 is valid under the zero temperature approximation (a reasonable approximation for IR detectors operating at 77K) and for thick metal films. Subsequently the IPE model was review by Elabd and Kosonocky in order to obtain better agreement with the experimental data.[25] Under the zero temperature approximation, they used the same formula in Equation 2, but with a slightly different expression for the quantum efficiency coefficient ($C=1/8\phi_B$). In particular they extended the photoemission model for thin metal films (with a film thickness much smaller than the attenuation length of carriers) by introducing a multiplicative gain factor - in order to take into account the increased escape probability of the photo-excited carriers into the semiconductor, because of the scattering at the metal surfaces.[25] Many authors have investigated IPE theory and new physical models have been proposed during the last few years.[26-28] Very recently Scales *et al.* [29] extended the theory proposed by Elabd and Kosonocky, deriving the escape probability through a double Schottky barrier.

One interesting approach is that reported by Vickers. He developed a model in which estimation of the internal quantum efficiency η_i of an IPE-based metal/semiconductor Schottky PD is based on the product of two factors [30]:

$$\eta_i = F(\phi_B) \cdot P(d) \quad (3)$$

where F (named the Fowler factor) is the fraction of the excited carriers having appropriate momentum and energy to overcome the potential barrier and P is a scattering term that takes into account the probability that one of these excited (hot) carriers will be emitted over the Schottky barrier after scattering by cold carriers and the metal boundary surfaces. In addition, d and ϕ_B are the metal thickness and junction potential barrier, respectively. The advantage of the Vickers' theory is that its derivation removes the zero temperature approximation. Indeed, the factor F incorporating the temperature dependence is shown in the following formula:

$$F = \frac{1}{4E_F h\nu} \left(\frac{(h\nu - \phi_B)^2}{2} + (k_B T)^2 \left\{ \frac{\pi^2}{6} + \sum_{i=1}^{\infty} \frac{1}{i^2} \left(-e^{-\frac{h\nu - \phi_B}{k_B T}} \right)^i \right\} \right) \quad (4)$$

where k_B and T are the Boltzmann constant and the absolute temperature, respectively. It is worth noting that, in the limit $T \rightarrow 0$, Equation 4 reduces to the more well-known Equation 2. Very recently Casalino showed that Equation 4 can be approximated at room temperature by the following equation (Equation 5) [31]:

$$F = \frac{1}{8E_F h\nu} \left((h\nu - \phi_B)^2 + \frac{(k_B T \pi)^2}{3} \right) \quad (5)$$

within 10% when $h\nu - \phi_B \geq 0.035$ eV, within 5% when $h\nu - \phi_B \geq 0.046$ eV - and within 1% when $h\nu - \phi_B \geq 0.074$ eV.

The scattering term, P , takes into account the extension of the photoemission theory to a thin film - where the probability of emission into the semiconductor of carriers excited in the metal

is increased. Indeed, Vickers derived the very simple approximate analytical formulation (Equation 6) [30]:

$$P = \frac{L^*}{d} \cdot \sqrt{1 - e^{-\frac{d}{L^*}}} \quad (6)$$

where L^* is the mean free path in the metal (due to the probability of collision of excited carriers with cold carriers and the two metal boundaries) and d is the metal thickness. Equation 6 is valid for thin films (in the limit $d/L^* > 0.2$). Very recently Casalino showed that, by slightly modifying Equation 6, it is possible to extend the operating range to very thin films (in the limit $d/L^* > 0.002$).[31] In any case, the lower the metal thickness the higher the scattering term P and so the higher the efficiency. This result is interesting because it has recently been proposed that the metal should be replaced by a two-dimensional material such as graphene.[16] Finally it is worth mentioning that a lower Schottky barrier height (SBH) can be obtained by applying a reverse bias through the junction - due to image force effect.[32] The SBH lowering depends on the square root of the reverse bias and its reduction can be used to increase the device efficiency, as shown in Equation 2.

3.2. Two-photon absorption (TPA)

Two-photon absorption (TPA) is a nonlinear optical process where, in a semiconductor, an electron can be moved into an excited state by the simultaneous absorption of two photons of identical wavelength (for the degenerate configuration). Because the transition energy for this process is equal to the sum of the energies of the two absorbed photons an electron-hole pair is generated if the energy of the photons is equal to or greater than half the energy bandgap of the semiconductor. In consequence, within the wavelength range of silicon transparency ($\lambda > 1.1 \mu\text{m}$), the sum of the energies from the two photons, even if it is insufficient to excite an electron across the direct bandgap of silicon ($E_{gd}=3.4\text{eV}$), may be sufficient to excite an electron across the indirect band-gap of silicon ($E_{gi}=1.12 \text{ eV}$). In Figure 2, the degenerate TPA process in silicon is illustrated schematically. In order to reach the final state, no

intermediate state is necessary, only a “virtual state” that does not correspond to any electronic or vibrational energy eigenstate. However, conservation of momentum requires that the indirect TPA transitions must be assisted by phonons. In phonon-assisted TPA, the phonon interaction can occur either during the absorption of the first photon or within the fleeting lifetime of the virtual state of the electron that exists after absorption of the first photon.

The TPA process can be evaluated through the TPA coefficient β , which is related to the imaginary part of the third-order susceptibility $\chi^{(3)}$; i.e. the lowest order of the silicon optical non-linearity, because of the centro-symmetry of the silicon crystal. In particular:

$$\beta(\omega) = \frac{3\pi}{c\epsilon_0\lambda n_0^2} \text{Im}\{\chi^{(3)}\} \quad (7)$$

where n_0 is the linear refractive index, ϵ_0 is the vacuum permittivity, and λ is the wavelength of the optical beam.

A wealth of experimental and theoretical work regarding the estimation of the degenerate TPA coefficient and its spectral dependence in silicon has been carried out - and several review papers have reported a comprehensive picture of all these data.[33-35] In particular, Figure 3 shows the experimental TPA coefficient for silicon collected by Hon *et al.* [34] - where the data points are determined from Refs. [36-47].

Figure 3 shows clearly that TPA drops rapidly when the wavelength is tuned beyond 1.7 μm and becomes negligible when the wavelength is tuned beyond 2.2 μm (corresponding to the half band gap of silicon). Two dispersion curves, one fitted to the data collected by Bristow *et al.* [44] and the other fitted to the data measured by Lin *et al.* [45], are plotted in Figure 3. These curves set upper and lower boundaries on the results reported in the literature and can be determined using a model related to the indirect optical transition processes [48, 49]; in particular $\beta(\omega)$ can be given as:

$$\beta(\omega) = \frac{2\pi C}{(2h\nu/E_{ig})^5} \sum_{m=0,1,2} \left[\frac{(2m+1)!!}{2^{m+2}} (m+2)! (2h\nu/E_{ig} - 1)^{m+2} \right] \quad (8)$$

where C is a material-dependent material, and $m = 0, 1$, and 2 is related to the transition process.[48] Lotshaw *et al.* [50] determined the effect of the doping concentrations in silicon and these results are illustrated in Figure 4 - whereas O'Dowd *et al.* [51] have made detailed measurements of the dependence of β on the state of polarisation.

The TPA coefficient allows evaluation of the TPA-induced free-carrier density. In particular, for an integrated silicon-based optical device, the free-carrier density $N(z)$ at position z is given by [52]:

$$N(z) = \beta \frac{\lambda \tau_{eff}}{2h\nu} \frac{P^2(z)}{A_{eff}^2} \quad (9)$$

where $P(z)$ is the propagating power at position z , λ is the wavelength of the optical beam, $h\nu$ is the photon energy, A_{eff} is the effective area of the waveguide - and τ_{eff} is the effective free-carrier lifetime. The last parameter depends on the geometry and size of the silicon waveguide. In particular, for sub-micrometric waveguide sizes, the lifetime is largely determined by surface recombination – which is fabrication process dependent. Generally, values in the range from 55 ps to 100 ns have been reported.[53-54] The values of β given in Figure 3, together with the tight mode confinement provided by the silicon waveguides, make the free-carrier generation induced by the two-photon absorption in the transparent regime sufficient. The TPA-induced free carriers can be drifted away by means of an external electric field, giving the possibility of implementing a square-law photodetector. However, if a high optical intensity is used, free-carrier accumulation can occur [55] - affecting the transmission along the optical waveguide. In fact, free carriers induced by TPA give rise to optical absorption and the plasma dispersion effect, according the well-known equations [56]:

$$\begin{aligned}\alpha_{TPA} &= \frac{e^3 \lambda^2}{4\pi^2 c^2 \epsilon_0 n} \left(\frac{\Delta N_e}{m_{ce}^2 \mu_e} + \frac{\Delta N_h}{m_{ch}^2 \mu_h} \right) \\ \Delta n_{TPA} &= \frac{e^2 \lambda^2}{8\pi^2 c^2 \epsilon_0 n} \left(\frac{\Delta N_e}{m_{ce}} + \frac{\Delta N_h}{m_{ch}} \right)\end{aligned}\quad (10)$$

where e is the electronic charge, n is the refractive index of unperturbed silicon, m_{ce} (m_{ch}) is the effective mass of conduction electrons (holes) - and μ_e (μ_h) is the electron (hole) mobility. As a result, the evolution of the optical signal intensity, during propagation inside a waveguide, may be described as:

$$\frac{dI}{dz} = -\alpha I - \alpha_{TPA} I - \beta I^2 \quad (11)$$

where α is the linear loss coefficient. In the design of a TPA-based PD, the foregoing coupled set of equations must be solved numerically to obtain the transmitted energy and to estimate the critical power level, above which TPA-generated free-carrier absorption effects are significant, as compared with TPA.

3.3. Bulk defect-mediated absorption (BDA)

Lattice defects have associated deep-level charge states within the silicon bandgap, which provide a mechanism for linear optical absorption of sub-bandgap wavelengths. For instance, a deep level having a charge-state energy located E_{dl} below the conduction band can provide electron-hole-pair generation through the two-step process depicted in Figure 5a. Firstly, the absorption of a photon with energy $h\nu > E_g - E_{dl}$ (where E_g is the bandgap energy) excites an electron from the valence band into the deep level. Secondly, the electron is thermally excited from the deep level into the conduction band.[57]

The absorption signature of silicon defects was first demonstrated using neutron damaged silicon by H. Y. Fan and A. K. Ramdas in 1959, which produced a peak response at 1.8 μm wavelength - as shown in Fig. 5b.[58] This 1.8 μm absorption band was later associated with the neutral divacancy at energy $E_{dl} = 0.4\text{eV}$, which produces photoconductivity for low dose ion-implanted silicon.[59, 60]

Lattice defects can be introduced in a controlled manner using ion implantation. Silicon waveguides that have undergone H^+ and Si^+ ion implantation processes produce excess optical losses at 1550 nm, which can be attributed to the tail of the 1.8 μm divacancy absorption spectrum.[61-63] The excess optical loss gradually reduces after thermal annealing treatments of temperatures above 200°C - and is completely removed at 350°C [63], where the divacancy is known to disappear.[64] Excess loss that persists following anneals at 475°C indicates the presence of another stable defect: the interstitial cluster.[65, 66] The electronic state of this defect, measurable through its associated excess optical loss and photocarrier generation, has been shown to be reversibly modified by current injection.[67]

3.4. Surface defect-mediated absorption (SDA)

In addition to deep levels formed in the silicon lattice, surface states are formed by the dangling bonds at silicon interfaces, which produce mid-bandgap energy levels that provide a pathway to absorption of sub-bandgap wavelengths. The excess optical loss from a silicon surface was reported, by Chiarotti *et al.*, to reach a peak at a photon energy of 0.5 eV - and to be removed following oxidation of the surface.[68] Local removal of the silicon dioxide cladding on silicon waveguides has been demonstrated to produce photocarrier generation from guided C-band wavelengths.[69, 70] Similarly, deposited polycrystalline-silicon has dangling bonds at the grain boundaries, leading to a distribution of deep levels that are 0.65 eV below the conduction band [71] - and have been shown to provide sensitivity to C-band wavelengths.[72]

4. Infrared all-silicon sub-bandgap photodetectors

In this section, a review of recent milestones in the development of all-silicon sub-bandgap PDs based on the aforementioned physical effects will be provided.

4.1. IPE-based PDs

IPE-based PDs have been widely investigated over the last few years. Devices based on Si nanoparticles, metal stripes supporting surface plasmon polaritons (SPPs), antennas and metallic gratings, have been reported. In addition, new Si structures based on the addition of two-dimensional materials such as graphene have shown very promising results. [16]

4.1.1. Surface-illuminated and waveguide-integrated PDs

IPE-based surface-illuminated PDs are inherently less responsive than IPE-based waveguide PDs - where the optical power can be confined at the metal-semiconductor interface. On the other hand, waveguide structures are not suitable in cases where surface-illuminated devices are the only option: for instance, in imaging applications - where the vision can be improved in critical conditions such as smoke and fog thanks to reduced scattering at NIR wavelengths [73], or in reflectography applications where the transparency of most pigments to NIR wavelengths has been used to investigate ancient paintings.[74] In addition surface-illuminated Schottky PDs have been used in the field of Schottky-barrier infrared focal plane array (FPA) technology that has evolved through the marriage of silicon-based IR detectors and charge coupled device (CCD) multiplexers.[75]

The most popular Schottky-barrier detector is the PtSi detector, which can be used for detection in the 3–5 μm spectral range.[76] PtSi detectors have been characterized by two main drawbacks: low quantum efficiency (of the order of 1%) and low operating temperature (of the order of 77 K). In order to overcome these drawbacks, Casalino *et al.* proposed, in 2006, to incorporate a Schottky junction inside a Fabry-Perot optical microcavity - in order both to increase the detection efficiency at near-infrared wavelengths and to give operation at room temperature.[77, 78] After a first experimental proof-of-concept demonstration [79, 80], the same authors, in 2012, fabricated and characterized a device that used a resonant cavity Fabry-Perot structure. The device was formed by a dielectric bottom mirror, a metallic top mirror and, in the middle, a silicon cavity space.[81] The dielectric bottom mirror was a

distributed Bragg reflector (DBR) formed by alternating $\lambda/4$ -layers of amorphous hydrogenated silicon (a-Si:H) and silicon nitride (Si_3N_4) while the top mirror was realized by means of a copper (Cu) layer that worked both as an absorber and as an optical mirror, at the same time. It was demonstrated that, when critical coupling conditions are fulfilled, i.e., when the DBR mirror reflectivity approaches the reflectivity of the metallic top mirror, maximum responsivity is obtained at the cavity resonance wavelengths. Critically coupled devices exhibit a maximum responsivity of 0.063 mA/W around 1550 nm and, moreover, junction capacitance measurements (pF) encourage the pursuit of greater bandwidth - with several GHz operation being possible. The dark current (density) is reported to be as high as 3.5 mA (28 mA/cm^2) at -1V. More recently, B. Desiatov *et al.* [82] have demonstrated an improved configuration in a surface-illuminated Aluminum(Al)/Si Schottky PD for the near-IR wavelength band - based on pyramidally shaped devices created in Si by potassium hydroxide (KOH) etching. The advantage of KOH etching is that it has the ability to fabricate plasmonic Si PDs with a nanometric active area, without needing sophisticated tools such as focused ion beam (FIB) or electron beam lithography (EBL). On the other hand, the Si pyramids, arranged in an array structure, perform as efficient and broadband light concentrators, collecting the light from a large area into a small active pixel area, thereby providing high responsivity, together with low dark current. The device responsivity versus incident optical power at 1550 nm is shown in Figure 6.

The responsivity of the device at -0.1 V was found to be 5, 12 and 30 mA/W - for incident optical wavelengths of 1550 nm, 1300 nm and 1064 nm, respectively. In addition, the device showed a dark current of 80 nA at -0.1 V. It is claimed that the efficiency of the photo-emission process is enhanced not only by the increased absorption but also by the nanoscale apex of the pyramid contributing to an increase in the emission probability of electrons from Al into Si. In 2008, Zhu *et al.* [83] described the first nickel silicide (NiSi) Schottky PD

integrated into a silicon-on-insulator (SOI) waveguide working at NIR wavelengths and at room temperature. Responsivity, bandwidth and dark current values of 4.6 mA/W, 2 GHz and 3 nA, respectively, at -1 V were reported. A similar device from the same research group, but based on a metal-semiconductor-metal (MSM) configuration shows both higher responsivity and greater dark current.[84] While, in the aforementioned guiding structures, the absorbing metal is deposited along the direction of the propagating light, this new structure featured an active copper (Cu) layer placed on the vertical exit surface of the output waveguide, i.e., normal to the propagating beam.[85] This proposed PD design is based on an asymmetric metal-semiconductor-metal (MSM) junction integrated on to a silicon-on-insulator (SOI) substrate. The main novelty of the structure is that, with the Cu layer being in contact with Si only on the vertical exit wall of the optical waveguide, it works as a mirror (as well as an active absorbing layer), enabling the possibility of fabricating an integrated cavity if a second mirror is fabricated on the waveguide (for instance by means of deep trenches). A substantial shrinking of the footprint of the detector - and an increase in the device performance could be obtained in this case. The integrated PD was characterized by a responsivity value at 1550 nm of 0.08 mA/W and a dark current of 10 nA, at -1 V. In 2013, Casalino *et al.* proposed an optimized version of this device that is capable of tackling a typical responsivity/dark current trade-off, impacting on the performance of IPE-based devices (Figure 7a). In Ref. [86], it was shown that taking advantage of a small contact area of about $3 \mu\text{m}^2$, it was possible to increase the magnitude of the applied reverse bias voltage to as much as 21 V, while maintaining a very low dark current of only 2.2 nA. The increase in reverse voltage reduces the Schottky barrier height (due to the image force effect [32]) – and increases the responsivity to 4.5 mA/W, as shown in Figure 7b. In addition an experimental bandwidth of 1 GHz was demonstrated (inset of Figure 7b).

In addition, the Schottky PD proposed has the potential to work at longer wavelengths than

the NIR (i.e. wavelengths in the range 2 to 3 μm – or longer).[86] Although some IPE-based Schottky PDs integrated with microring resonators have been investigated theoretically in the literature [87, 88], no experimental validation has been carried out to so far. A very interesting in-line, IPE-based, Si PD was reported in Ref. [89], where an Au Schottky layer was placed directly on the Si core of a non-conventional optical fiber. This Si-cored fiber was fabricated by starting from polycrystalline n-type Si powder, firstly packed in a fused silica tube and then melted at an appropriate temperature.[89] The authors report a responsivity and dark current combination of 0.226 mA/W and 0.3 μA , respectively, at -0.45 V for a wavelength of 1550 nm. This device could be very interesting in the field of Lab-on-Fiber technology.

4.1.2. Surface plasmon PDs

Silicon surface plasmon PDs are based both on the integration of a Schottky detector with a Si waveguide and on the excitation of a surface plasmon polariton (SPP).[90] Indeed, while the SPP mode propagates along the metal stripe deposited on the Si optical waveguide, it is absorbed - making the sub-bandgap detection possible by emission of carriers into Si, in agreement with the typical internal photoemission mechanism. The group of P. Berini has investigated, from both a theoretical [91] and an experimental [12] point of view, the performance, at 1550 nm, of Schottky diode PDs integrated into a metal stripe that supports SPPs.

A candidate structure was fabricated as an Au stripe on p-Si, forming a Schottky contact.[12, 13] The sa_b^0 mode [90] localized at the Au/p-Si interface was excited at NIR wavelengths - under both end-facet and top illumination, as shown schematically in Figure 8. Figure 8(b) plots photogenerated current (I_p) versus incident optical power (S_{inc}), under the best alignment conditions. Under end-facet illumination, the measured responsivities were almost identical at 0.942 and 0.941 mA/W at -0.1 V in an asymmetric 1.5- μm -wide 40- μm -long 40-nm-thick Au

strip waveguide at wavelengths of 1310 nm and 1550 nm, respectively. On the other hand, under top illumination, the measured responsivity was 0.559 mA/W at -0.1 V in an asymmetric 6.5- μm -wide 40- μm -long 40-nm-thick Au strip waveguide, at 1550 nm. The device dark current was in the μA range. Previously, the same authors reported on a similar device (2.5- μm -wide. 75- μm -long – and with a 135-nm-thick Au stripe on n-Si) - working under a strong reverse bias that approaches the breakdown condition (-210 V) and showing a responsivity of 2.35 mA/W at 1550 nm.[92] The aforementioned devices are all based on asymmetric cladding configurations. Some theoretical studies involve a symmetric cladding configuration - where the metal stripe is buried in Si [93, 94], thereby taking advantage of the increased emission that occurs through the use of two Schottky junctions.[29] Even though no experimental validation has been performed so far on symmetric cladding SPP Si PDs, M. K. Knight *et al.* [95] demonstrated increased responsivity for plasmonic nanostructures embedded into the Si semiconductor. Nanostructures, arranged into a 10 μm x10 μm array, were based on planar Ti/Au nanowires 2/35-nm-thick embedded in Si to a depth of 5, 15 and 25 nm in such a way that, not only the flat surface, but also the vertical surfaces of the planar nanowires were in contact with the Si. An increase in the photocurrent was observed (but no changes in the calculated absorbance), relative to non-embedded plasmonic elements, by embedding the nanowire just a few nanometers into the Si. Indeed, the responsivity exhibits a consistent increase in amplitude with increased embedding depth of the nanowire – and this trend was most clearly observable for the nanowires with the widest transverse dimensions. The highest aspect ratio (ratio of width to thickness) devices exhibited a measured photocurrent response around 25 times greater than the non-embedded structures. The maximum reported responsivity was 65 $\mu\text{A/W}$ at 1550 nm, for incident light polarized transverse to the length of the nanowire. The authors attribute the responsivity enhancements to the increased carrier probability emission occurring through the three metal/Si interfaces.

In the 2012, I. Goykhman *et al.* demonstrated a Si Schottky PD for telecom wavelengths that was integrated with a nanoscale Si bus waveguide.[96] The device was based on an Al Schottky contact fabricated using the standard microelectronic LOCOS technique. The Al photoactive area in contact with the Si was 320 nm x 1000 nm - as shown in Figure 9. The PD was found to have an internal responsivity of 12.5 mA/W at 1550 nm and -0.1 V bias, with a leakage current on the order of 30 nA.

This responsivity is about two order of magnitude higher than that reported by the same authors for a similar device two years earlier.[97] The authors attribute the enhanced responsivity to the presence of surface roughness at the boundary between Al and Si. In the same year Zhu *et al.* demonstrated a waveguide all-Si PD based on nickel silicide nanoparticles embedded in the space charge region of a p-n Si junction.[11] While the idea of enhancing the IPE by using nanoparticles (NPs) is not completely new [98, 99], the previously reported structures were only able to work at cryogenic temperatures (77 K) and at wavelengths shorter than those typically required for telecom and datacom applications.[100, 101] The enhanced responsivity of PDs based on NPs is typically attributed both to the increased light absorption through excitation of localized surface plasmon resonance (LSPR) on the silicide NPs and to the increased emission probability of the photo-excited carriers associated with the spherical shape of the NPs.[102] The structure proposed in Ref. [11], which is capable of working at both room temperature and a wavelength of 1550 nm, exhibits significant ingenuity: the junction was realized starting from p-type Si. Firstly a ~1-nm-thick titanium (Ti) film and a ~3-nm-thick nickel (Ni) film were deposited, followed by a rapid thermal annealing (RTA) process at 200°C for 30 s, in order to produce nickel silicide (NiSi). After removing the un-reacted metal using a 90°C Piranha solution [103], a 200-nm thick film of amorphous Si (a-Si) was deposited, followed by phosphorus implantation and an RTA process at 700°C for 5 min - in order to obtain dopant activation. Moreover, during this

thermal process, the Ni-silicide agglomerates to form nanoparticles. Meanwhile, the a-Si layer crystallizes to form polycrystalline Si (polySi), due to the metal-induced crystallization effect. Finally, the p-Si and n-polySi were connected by Al electrodes to form a p-n diode.

The device provides a responsivity at room temperature that depends on both wavelength and polarization, and it peaks at 30 mA/W for -5 V and TE polarization. Finally, a bandwidth and dark current density, respectively, of 6 GHz and 2.84 A/cm² at -5V were reported. Schottky photodiodes consisting of Au nanorods randomly distributed on a 30-nm-thick Au film on a Si substrate have been reported in Ref. [104]. The length of the nanorods was 50 to 100 nm and their diameter was 10 nm. The authors claim that the Au nanorods induce SPR under illumination at 1300 nm and 1550 nm - producing enhanced photocurrent via IPE with respect to the same devices without nanorods. Measurements were performed without bias. In 2011, Knight *et al.* [14] reported on the excitation of resonant plasmons in metallic nanoantennae, in order to achieve strong optical absorption in a small PD active region. The device consisted of three hundred nanoantennas arranged in a 15 x 20 array. Each nanoantenna used 30-nm-high and 50-nm-wide rectangular Au nanorods - and their lengths ranged from 110 to 158 nm. A thin titanium (Ti) adhesion layer was used between the Au contact layer and the n-Si. The device responsivity depends on the complex optimization of several factors (the properties of the materials involved, the geometry and the efficiency of the uppermost indium tin oxide electrical contact layer) Low responsivity values of 10 μ A/W at 1250 nm and 3 μ A/W at 1550 nm without reverse bias, have been reported so far. Another approach to obtaining plasmon-induced hot electron generation was proposed by A. Sobhani *et al.* [15] and is based on the phenomenon of extraordinary optical transmission (EOT) in metallic gratings. The same plasmon modes that give rise to EOT also give rise to hot electrons that can be emitted into a semiconductor substrate through a properly designed Schottky barrier. Au gratings with different geometries were fabricated on n-type Si by using Ti as adhesion layer – and

demonstrated a maximum responsivity value of 0.6 mA/W at 1300 nm and about 0.47 mA/W at 1500 nm, for zero bias voltage. Device measurements showed a drastic increase in responsivity with respect to structures based on nanoantennas. This increase in responsivity arises from the fact that it is possible to design the grating geometry in such a way as to generate hot electrons primarily near the Schottky interface. In addition, the main advantage of this approach is that by changing grating geometry it is possible to linearly tune the responsivity peak over a broad wavelength regime ranging from 1295 and 1635 nm.

In the 2014, M. A. Nazirzadeh *et al.* [105] demonstrates Si Schottky PDs for broad-band NIR detection in 1200-1600 nm wavelength range based on Au nanoisland able to plasmonically enhance the sub-bandgap photon collection and generate photocurrent by IPE. Randomly distributed Au nanoisland on Si surface are fabricated by depositing a continuous thin Au layer and then annealing it at 300°C, 450°C and 600°C. The device annealed at 450 °C had the highest responsivity at 1300 nm of 2 mA/W and its dark current is about 30 μ A at -1 V. On the other hand, device annealed at 300 °C had the highest responsivity at 1550 nm of 0.6 mA/W and its dark current is about 100 μ A at -1 V. The advantage of the proposed device is that all nanostructures are realized without any high resolution lithography technique.

4.1.3. PDs based on Graphene/Si Schottky junctions

Extensive investigations have been performed on graphene since its discovery in 2004.[106] Electrons in graphene behave as massless two-dimensional particles; this structure leads to a significant absorption from ultraviolet to infrared through inter-band and intra-band transitions.[107, 108] This property is of paramount importance in the field of the photodetection where devices realized by semiconductor materials have a limited detecting spectral width; for this reason graphene-based PDs are presently one of the most investigated photonic devices in a broadband range of wavelengths, in particular at NIR. Graphene forms a Schottky junction with Si [109] and due to its two-dimensionality it is a good candidate for

the realization of IPE-based PDs. In the 2013 M. Amirmazlaghani *et al.* reported on an exfoliated graphene/Si Schottky PD working at 1550 nm.[16] Experimental results show a responsivity ranging from 2.8 to 9.9 mA/W at 1550 nm depending on the reverse voltage applied. The maximum responsivity of 9.9 mA/W was obtained at -16 V where measured dark current is about $2.4 \mu\text{A}$. Authors show that measured responsivity is higher than the theoretical predicted by commonly used Equation 2. Authors explain this discrepancy by claiming that physics of IPE totally changes in Schottky junction involving two-dimensional materials in particular concerning emission probability of carriers from graphene to Si that results increased. Very recently Goykhman *et al.* demonstrated an on-chip, waveguide-integrated, silicon-graphene (grown by chemical vapor deposition) Schottky PD operating at 1550 nm.[110] The device is based on a rib waveguide realized on a SOI substrate where the rib is coupled to a single layer graphene (SLG)/Au contact that electrically forms a Schottky junction, while supporting surface plasmonic mode able to confine the optical beam at the interface where IPE process takes place. The PD length is $\sim 5 \mu\text{m}$ and the Si waveguide width is 310 nm. Authors show an internal responsivity of 85 mA/W at -1 V reverse bias with a dark current of 20 nA. Internal responsivity increases up to 0.37 A/W at -3 V and authors attribute this increase to the combined effect of two processes: thermionic-field emission (TFE), i.e., tunneling through the graphene/Si Schottky junction [111] and avalanche multiplication of photoexcited carrier inside the Si depletion region.

Finally, Vabbina *et al.* recently published a very interesting IPE-based two-dimensional PD operating at 1440 nm.[112] Proposed device consists in a thin p-type molybdenum disulfide (MoS_2) with graphene to form a MoS_2 /graphene Schottky PD where photo generated holes travel from graphene to MoS_2 over the Schottky barrier under illumination. MoS_2 is a unique two dimensional semiconductor material with a direct bandgap ($E_g^{\text{MoS}_2}$) of 1.80 eV. The graphene/ MoS_2 multilayer was deposited on a oxidized Si substrate. Sputtering-CVD

technique was employed to synthesize a few layers of MoS₂ [113] while the CVD process is used to synthesize graphene.[114] Authors found that the p-type MoS₂ forms a Schottky barrier with graphene of 139 meV. Proposed device is shown in Figure 11a.

The spectral responsivity, measured at –2 V reverse bias, is shown in Figure 11b. When the PD is operated in energy gap excitation mode ($h\nu > E_g^{MoS_2}$) a maximum responsivity of 0.52 A/W is observed at 590 nm. Beyond 670 nm, where the incident photon energy is smaller than $E_g^{MoS_2}$, the photo current is due to IPE from graphene to MoS₂ and a maximum responsivity of 1.26 A/W at -2 V and a noise equivalent power of 7.8×10^{-12} W/ $\sqrt{\text{Hz}}$ at 1440 nm, were obtained. The reported dark current is about 300 μA at -2 V.

4.2. TPA-based PDs

The proportionality of $N(z)$ to the propagating optical power (Equation 9), allows using the TPA process for implementing a square-law detector. The free carriers induced by TPA can be drifted away by means of a p-i-n diode. However, due the low value of the TPA coefficient, a high optical power is required to initiate the nonlinear process and thus achieve a high responsivity.[115] In order to realize photodetectors with a relatively low input optical power, an effective area of the waveguide as small as possible should to be realized (see Equation 9). Paniccia's group [116] has used this approach in order to integrate a power-monitoring device in a passive silicon waveguide. In particular, a rib waveguide was 600nm wide by 500nm high, with an etch depth of 220 nm. The small waveguide cross-section allowed inducing TPA-generated free-carriers at a continuous-wave regime of few mW of optical power. Thus, the optical loss induced by TPA during the optical propagation inside a waveguide can be considered negligible. The TPA-induced free carriers were extracted from the waveguide with p-i-n structures realized in different points of the waveguide. In Figure 12a the cross-section of the rib structure with the integrated p-i-n diode is illustrated. The

measured TPA-generated current (I_{TPA}), as a function of optical power inside the silicon waveguide, (P_{in}), for three different reverse-bias conditions is shown in Figure 12b.

By means of this approach the authors were able to accurately determine the waveguide propagation loss. In fact, they positioned a p-i-n diode both at the input and output of a rib waveguide and extracted the propagation loss coefficient directly from the measured output and input TPA-induced currents. The evaluated data was consistent with a separate measurement performed with the conventional cutback method. A further enhancement of TPA process has been achieved adopting optical microresonators, such as rings, disks, and photonic crystal cavities. Ultrafast photodetection based on this approach has been demonstrated both experimentally and theoretically.[117-126] Zhu *et al.* [126] have recently studied the effect on the TPA-induced current of the placement of the p-n junction with respect to the whispering gallery modes excited in a silicon microdisk resonator. In Figure 13a the schematic drawing of the proposed structure is reported.

The authors studied the current generation due to three resonance modes (TE₀, TE₁, and TE₂) and for two different positions of the p-n junction with respect to the optical modes. In particular, in device I the junction electric field has a good coverage over the TE₀ mode, while in device II it has a good coverage over the TE₁ mode. The current generated by the three modes as a function of on-chip optical powers are illustrated in Figure 13b for device I and Figure 13c for device II. It's interesting to note that at high optical power, the increment of current for TE₀ in device I and TE₁ in device II gradually slows down, because of the free-carrier absorption induced by the strong TPA effect (see Equation 10). Data reported in Figure 13 were obtained with a low reverse bias voltage (-3V) in order to avoid the avalanche effect. Furthermore, the authors showed that a significant enhancement of the responsivity can take place if the devices operate in avalanche regime. In fact, they measured a responsivity larger than 1A/W with an optical power of 44.7 μ W and a reserve bias larger than -22V. However, a

trade-off between the enhanced responsivity and a larger dark current has to be taken into account.

One of the main drawbacks of the structures based on microcavities is their narrow bandwidth. Baba's group [127] have proposed to widen the operating bandwidth of TPA-based photodetector by employing lattice-shifted photonic-crystal waveguides (LSPCWs).[128-130] An image of the proposed device is illustrated in Figure 14a.

The photonic crystal structure allows slowing down the speed at which an optical pulse envelope propagates inside the waveguide (group velocity). Thanks to this reduction, the light-matter interaction increases and, additionally, a spatial compression of the pulse energy is achieved, increasing the peak of the electric field intensity carried by a slow light pulse. Both the mechanisms induce an enhancement of the silicon nonlinearity.[128-130] The lattice-shifted Si photonic crystal waveguide allows keeping a low group velocity together with a wideband low dispersion. Figure 14b indicates the photocurrent due to TPA effect. The deviation from the expected quadratic dependence at low powers is due to the high signal-to-noise ratio, whereas at high powers it is due to the free-carrier absorption induced by the strong TPA effect. The responsivities at maximum incident powers were 0.023, 0.043, and 0.052 A/W for $n_g = 16$, 20, and 24, respectively.

4.3. SDA and BDA-based PDs

A recently popular technique for producing all-Si PDs in an otherwise transparent photonic circuit has been to locally enhance SDA or BDA absorption. The processing methods used to actualize a controlled enhancement of these effects and the PD structures that have been shown to derive maximum benefit from it are described in this section.

4.3.1. In-line waveguide photodiodes

The first photodiode structures used to exploit photocarrier generation from bulk defects was a ridge waveguide with doped p^+ and n^+ regions on either side to form a lateral P-I-N diode as shown in Figure 15a.[61] These dopant regions are positioned sufficiently far from the

ridge to produce negligible excess free-carrier absorption. The defects are added by a masked high energy (200 keV – 1.5 MeV), low dose (10^{12} - 10^{14} cm⁻²) ion implantation back-end process. Demonstrations of defect formation to produce sensitivity to C-band wavelengths have used ion implantation with various species, including H⁺ [61], Si⁺ [62, 65], He [132], B⁺ [133, 134], Se [135], and Ar [136]. This effect was first demonstrated by Bradley *et al.* using a large (15 μ m² x 6 mm long) ridge waveguide structure similar to Figure 15a, where H⁺ implantation increased the optical loss by 13 dB/cm and produced 3 mA/W responsivity at 1550 nm wavelength.[61]

The implanted photodiodes are often subjected to a 200-475°C anneal for several minutes, which partially repairs the lattice damage and therefore modifies the defect type and concentration. Due to the carrier trapping properties of the point defects, the photodiode responsivity is maximized at intermediate annealing temperatures, despite having lower excess optical loss.[61, 62, 132] The optimum defect concentration is determined by the competing influences of optical carrier generation and carrier extraction efficiency.[57]

Geis *et al.* significantly improved the photodiode response by using a waveguide P-I-N diode of much smaller (0.1 μ m²) cross-sectional area (shown in Fig. 15b). Low doped *p* and *n* regions confine the electric field to within the waveguide, which reduces carrier transit time and improves carrier extraction efficiency. These devices exploited the interstitial cluster defect absorption, which dominates following a 475°C anneal. This enabled (external) responsivities of 0.2-5 A/W and bandwidths of up to 35 GHz [67], demonstrating a competitive photodiode for high speed telecom and datacom applications. As shown in Figure 16, the system performance has since been confirmed by Grote *et al.* with a demonstration error-free (BER< 10^{-12}) operation at 10 Gb/s with this structure [137], and by Korn *et al.* with open eye diagrams at 35 Gb/s.[138] In addition to the P-I-N photodiode structure, ion-

implanted photodiodes in a MSM structure have also been demonstrated with high responsivity (>0.5 A/W).[139]

Naturally existing surface states at the Si-SiO₂ waveguide interface have been exploited to provide sensitivity to C-band wavelengths, which provide significant absorption due to the large overlap of a sub-micron waveguide surface with its optical mode field.[140] The removal of the cladding oxide above the waveguide increases the number of dangling bonds [69], and was shown to increase the waveguide loss by 3 dB/cm and enhance the responsivity by 100× (relative to a sample with oxide cladding) to 45 mA/W.[70] The selective cladding removal is a standard CMOS-compatible process that can be used to induce photosensitivity in selected waveguide sections. Zhu *et al.* further exploited this surface state absorption using the enhanced electric fields in an interleaved pn junction diode.[141] Also, defect states have been reported in devices formed of deposited silicon, and was attributed to trap states associated with dangling bonds in the grain boundaries.[72] In both surface states arising from waveguide sidewall and grain boundaries, high speed (>2.5 Gb/s) operation was observed.[70, 72, 141]

In-line photodiodes of this type have now been utilized in several integrated photonic circuit functions. They are well-suited for power monitoring, when designed to absorb a small fraction of light at different positions in a circuit, particularly for control circuit applications.[142] This broadband and polarization-independent power sampling provides an attractive alternative to power tapping using a waveguide coupler. They have been used in this capacity in optical channel leveler circuits [133], modulator resonance alignment and stabilization circuits [143, 144], OSNR detection [145] and wavelength monitoring.[146]

4.3.2. Resonant enhancement of defect-mediated absorption

A fundamental disadvantage with defect-mediated photodiodes is that, despite high internal quantum efficiency, their long absorption lengths make them ill-suited to operate as terminal

photodiodes. High bandwidths of 35 GHz can only be achieved with in-line device lengths of 100 μm , for which only 4.5% of the light is absorbed.[67] The low absorption levels, however, can be mitigated by resonance enhancement.

By incorporating bulk or surface defects into a ring resonator, the total cavity round-trip loss can remain sufficiently small to allow moderate to high Q resonances.[147-149, 140, 72, 150, 151] By designing the ring resonator to be critically coupled, the responsivity is enhanced several times due to the build-up of optical intensity in the ring on resonance.[150] Figure 17 illustrates some ring resonator photodiodes that have been demonstrated, as well as a typical photocurrent spectral response. The defects may be naturally occurring surface states at the Si-SiO₂ interface [140], interface states in polysilicon [72] or bulk defects formed by ion implantation.[147-152] Several groups have reported ring-based defect-mediated photodiodes to have responsivity in excess of 0.1 A/W.[147, 72, 149, 150] This is remarkable considering the P-I-N diode lengths inside the rings are on the order of 100 μm , and as a result have low capacitance. The 3-dB frequency of ring-based defect-mediated photodiodes has been measured to be 7 GHz using interstitial cluster defects [149] and 3.5 GHz using divacancy defects.[151] Despite the improved capacitance, the photon cavity lifetime imposes an additional frequency limitation that needs to be considered in design.

Ring-based photodiodes can be integrated with heaters for thermal tuning, enabling wavelength tunable detection across a large range.[147] Such photodiodes could be serially arranged on a single bus waveguide to form a multi-wavelength receiver architecture, where the filtering and photodetection for each channel is provided by a single device. In addition, Fard *et al.* have demonstrated their suitability for lab-on-chip applications, where a change in the refractive index of the surrounding environment produces a change in the resonance wavelength, which can be directly measured through the photocurrent.[152]

Resonance enhancement using smaller footprint cavity structures have been reported. Ackert *et al.* integrated photodiodes into high-Q microdisks of 10 μm diameter.[153] The photodiode may be further reduced in size by using a fabry-perot cavity.[154-156] Haret *et al.* demonstrated a photonic crystal cavity of 4 μm^2 area with MSM contacts, which utilized a very strong resonant enhancement of surface states to achieve 17 mA/W responsivity.[154] Mehta *et al.* demonstrated a P-I-N junction integrated with a photonic crystal cavity (shown in Figure 17d), achieving 0.31 A/W and 3 GHz bandwidth with a -30V bias.[156] A drawback of high Q cavities is that the optical intensity on resonance becomes so large that the silicon heating introduces an optical bistability in resonance wavelength.[156]

4.3.3. Avalanche gain

Silicon, a common material for low-noise APDs due to its high ionization coefficient ratio, can provide carrier multiplication within the waveguide layer. Geis *et al.* observed evidence of this with in-line photodiodes when operated at -15V bias.[65] Ackert *et al.* designed the device shown in Figure 18 to provide a sufficiently strong DC electric field in the thin slab regions to achieve impact ionization.[157] The non-uniform electric field causes the responsivity to gradually evolve from unity gain at the slight plateau below 10V bias towards a value of 4.7 A/W at 40V bias. The bandwidth of the 0.6 mm long device was 2 GHz up to 35 V bias, and then began to degrade at higher bias due to the limits of high multiplication factor. An open eye diagram was observed at 10 Gb/s.[157]

4.3.4. MIR Sensitivity

There has been recent interest in expanding the silicon photonics platform to function at longer wavelengths in the region of 2 μm [158, 159], in part to expand spectrum for optical communications.[160] While many competing hybrid photodetection solutions for C-band wavelengths can't be extended to longer wavelengths due to band-edge roll-off, all-Si photodiodes provide sensitivity that extends into this wavelength range. For instance, the peak

of the divacancy optical absorption spectrum that is used for C-band photodetection (shown in Figure 5b) is at 1.8 μm wavelength.

Error free performance at 1 Gb/s was demonstrated by Souhan et al for Si⁺ implanted P-I-Ns at 1.9 μm wavelength.[161] Later, the implantation dose and annealing conditions were varied to demonstrate 10 mA/W sensitivity at 2.2 μm wavelength.[162] Similarly, B⁺ implanted large cross-section waveguides were tested across 2-2.5 μm wavelength and the results are shown in Figure 19a.[163] Despite the higher defect absorption level at longer wavelengths, both Souhan and Thompson found the responsivity to be lower than its C-band value, but this was attributed in both cases to the poor mode confinement in the waveguide geometries that were designed for C-band operation.[162, 163] Souhan *et al.* de-embedded this effect to calculate an internal quantum efficiency of 2.7-4.5% at 2.2 μm wavelength, as shown in Figure 19b.[162]

Ackert *et al.* designed a defect-mediated APD with waveguide dimensions suitable for 2 μm wavelength operation.[134] The oxide cladding was etched above the waveguide and was implanted with B⁺ ions. A responsivity of 0.3 A/W was demonstrated for 2.02 μm wavelength and 27 V bias on a 0.2 mm long device. The capacitance-limited bandwidth was 15 GHz, enabling 20 Gb/s detection as shown in the eye diagram in Figure 19c.[134] These results confirm both the suitability of defect-mediated detectors for MIR wavelengths, and their capacity for high bitrate operation.

5. Summary and perspectives

In this work an overview of sub-bandgap all-Si PDs working at telecom and datacom wavelengths has been presented. Firstly, we have described the most commonly utilized detection mechanisms for photo-conversion in Si at sub band-gap wavelengths: the internal photoemission effect, two-photon absorption and defect-mediated absorption. Thereafter, a quantitative comparison of selected PDs proposed in the recent literature has been given and

summarized in Table I.

IPE-based PDs have mainly been realized for operation at telecom wavelengths - at 1550 nm, in particular. They are characterized by a large bandwidth capability, thanks to the unipolar nature of the Schottky junction. The main drawback of the IPE-based PDs is their limited external responsivity. Schottky PDs based on metals and silicides have been realized by taking advantage of nanoscale metallic structures, including: Si nanoparticles, metal stripes supporting SPPs, antennas and metallic gratings. In any cases the experimental responsivity at 1550 nm is on the order of some tens of mA/W. However new perspectives are opened up by replacing metal or silicides with new emerging ‘two-dimensional’ materials such as graphene. Indeed, Schottky PDs based on graphene have recently shown the potentiality to increase the responsivity into the A/W range. On the other hand, PDs based on the TPA effect exploit the dependence of the generated photocurrent on the square of the instantaneous optical intensity. Because the TPA-induced photocurrent is small, due to the low TPA coefficient, these PDs are generally used with pulsed optical signals; in particular for autocorrelation in pulse shape measurements, dispersion measurements and optical clock recovery. Therefore, by using the TPA effect, rapidly varying optical phenomena can be detected and measured without using high-speed electronics. However, recent technological improvements that make possible the reduction of the effective area of the waveguides, together with the possibility of adopting efficient optical microresonators, also enable the use of TPA-based PDs for optical power monitoring. Finally, BDA- and SDA-based PDs are now established as a popular and straightforward means of integrating all-Si photodetection into standard silicon photonics process offerings.[70] Their characteristic responsivity/bandwidth trade-off has mostly limited these devices to application as power monitors in control circuits. However, the combination of resonance enhancement and avalanche gain has recently broadened their possible application to competitive high-speed terminal PDs. In addition, these devices are uniquely suited for

operation at longer wavelengths in the region of 2 μm - and have been validated in recent work at this wavelength. In some cases, results for all-silicon sub-bandgap photodetectors are already comparable to the state-of-the-art Si-Ge devices currently employed in Si photonics [5, 7]. In consequence, all-silicon sub-bandgap photodetectors promise to play a key role in telecom and datacom applications.

Table 1. Summary of selected all-silicon sub-bandgap PDs at telecom and datacom wavelengths

Device	Detection mechanism	Device type	Size	Responsivity	Bandwidth	Dark current/Dark current density
Casalino <i>et al.</i> [81]	IPE	Surface-illuminated Fabry-Perot microcavity	100- μm -thick silicon cavity	0.063 mA/W @1550nm (-0.1 V)	GHz range (estimated)	3.5 mA (-1 V)
Desiatov <i>et al.</i> [82]	IPE	Surface-illuminated Si pyramids	Pyramid apex ~50 nm	5 mA/W @1550nm 12 mA/W @ 1300 nm 30 mA/W @1064 nm (-0.1V)	-	80 nA (-0.1 V)
Casalino <i>et al.</i> [86]	IPE	Waveguide	Active area ~3 μm^2	4.5 mA/W @ 1550 nm (-21 V)	1 GHz	2.2 nA (-21 V)
Berini <i>et al.</i> [12]	IPE	Au strip supporting SPPs	Asymmetric 1.5- μm -wide 40- μm -long 40-nm-thick strip	0.942 mA/W @1310 nm 0.941 mA/W @ 1550 nm (-0.1 V)	-	0.3 μA (-0.45 V)
Goykhman <i>et al.</i> [96]	IPE	Nanoscale bus waveguide	Al active area 0.32 μm x 1 μm	12.5 mA/W @1550 nm (-0.1 V) Internal responsivity	-	30 nA (-0.1 V)
Zhu <i>et al.</i> [11]	IPE	NPs supporting LPSR	Few nm NPs	30 mA/W @1550nm (-5 V for TE polarization)	6 GHz	2.84 A/cm ² (-5 V)
Knight <i>et al.</i> [14]	IPE	15 x 20 matrix of Au nanoantennas	30-nm-height 50-nm-width nanoantenna	10 $\mu\text{A/W}$ @1250 nm 3 $\mu\text{A/W}$ @1550 nm (No bias)	-	-
Sobhani <i>et al.</i> [15]	IPE	Au grating based on EOT	Different grating geometries (few hundreds of nanometers)	0.6 mA/W @1300 nm 0.47 mA/W @1500 (No bias)	-	-

Nazirzadeh <i>et al.</i> [105]	IPE	Au nanoisland	-	2 mA/W @1300 nm (450°C) 0.6 mA/W @1500nm (300°C)	-	30 μ A (-1 V, 450 °C) 100 μ A (-1 V, 300 °C)
Amirmazlaghani <i>et al.</i> [16]	IPE	Surface-illuminated graphene/Si	-	9.9 mA/W @1550 nm (-16 V)	-	2.4 μ A (-16 V)
Goykhman <i>et al.</i> [110]	IPE	Graphene integrated with a rib SOI waveguide	PD length ~5 μ m Si waveguide width ~310nm	0.37 A/W @1550 nm (-3 V) Internal responsivity	-	20 nA (-1 V)
Vabbina <i>et al.</i> [112]	IPE	Graphene/MoS ₂ Schottky PD on oxidized Si	-	1.26 A/W @~1550 nm (-2 V)	-	300 μ A (-2 V)
Geis <i>et al.</i> [65-67]	BDA	Si ⁺ , 190 keV, 10 ¹³ cm ⁻² , 475°C anneal for 2 min	520x220 nm waveguide, 0.25 - 3 mm long P-I-N	0.2 - 5 A/W @1550 nm (-20V)	>35 GHz	10-400 nA (-20V)
Ackert <i>et al.</i> [70]	SDA	Si-air interface (locally removed cladding)	500x220 nm waveguide, 2 mm long P-I-N	45 mA/W @ 1530 nm (-2V)	10 Gb/s operation	2 nA (-2V)
Zhu <i>et al.</i> [141]	SDA	surface states (Si-SiO ₂)	interleaved P-N junction in 1.5 μ m wide waveguide, 1.5-2.5 mm long	40 mA/W/mm @ 1550 nm (-10V)	11.5 GHz	180 nA/mm (-10V)
Souhan <i>et al.</i> [139]	BDA	Si ⁺ , 195 keV, 10 ¹³ cm ⁻² , 250°C anneal for 10 min	750x220 nm waveguide, 1mm long MSM	0.5 A/W @ 1550 nm (50V)	2.6 GHz (50V)	~30 μ A (50V)
Shafiiha <i>et al.</i> [149]	BDA	Si ⁺ , 185 keV, 10 ¹³ cm ⁻² , 475°C anneal for 2 min	~90 μ m P-I-N (15 μ m radius ring)	0.1 A/W @ 1550 nm (-2 V)	7 GHz	0.1 nA (-2V)
Doylend <i>et al.</i> [147]	BDA	B ⁺ , 350 keV, 10 ¹³ cm ⁻²	60 μ m P-I-N in racetrack	0.14 A/W @ 1550 nm (-10V)	-	0.2 nA (-10V)
Preston <i>et al.</i> [72]	SDA	polysilicon grain boundry interface states	~300 μ m P-I-N (50 μ m radius ring)	0.15 A/W @ 1550 nm (-13V)	1 Gb/s operation	40 nA (-13V)
Ackert <i>et al.</i> [151]	BDA	B ⁺ , 350 keV, 10 ¹³ cm ⁻² , 200°C anneal for 5 min	~125 μ m P-I-N (20 μ m radius ring)	0.023 A/W @ 1560 nm (-5V)	2.4-3.5 GHz	0.2 nA (-5V)
Fard <i>et al.</i> [152]	BDA	B ⁺ , 30 keV, 5x10 ¹² cm ⁻² , no anneal	~250 μ m P-I-N (40 μ m radius ring)	0.09 A/W @ 1550 nm (-10V)	-	17 nA (-10V)
Ackert <i>et al.</i> [153]	BDA	B ⁺ , 350 keV, 10 ¹³ cm ⁻²	~60 μ m P-I-N (10 μ m radius disk)	0.045 A/W @ 1560 nm (-3V)	-	0.1 nA (-3V)
Haret <i>et al.</i> [154]	SDA	interface states	MSM in photonic crystal cavity	17 mA/W @ 1610 nm (10V)	1 GHz	12 nA (10V)

Mehta <i>et al.</i> [156]	SDA	p-Si grain boundaries	8 μm long P-I-N in Quasi 1-D photonic crystal cavity	0.31 A/W @ 1550 nm (-30V)	2.9 GHz	30 nA (-30V)
Ackert <i>et al.</i> [157]	BDA	B+, 500 keV, $5 \times 10^{12} \text{ cm}^{-2}$, 200°C anneal for 5 min	600 μm long APD	3.7 A/W @ 1560 nm (-35V)	2 GHz (-35V)	$\sim 3 \mu\text{A}$ (-35V)
Souhan <i>et al.</i> [162]	BDA	Si+, 190 keV, 10^{13} cm^{-2} , 350°C anneal for 10 min	0.25 mm long P-I-N	7.2 mA/W @ 2.2 μm (-5V)	1.7 GHz (-20V)	$\sim 3 \text{ nA}$ (-5V)
Thompson <i>et al.</i> [163]	BDA	B+, 4 MeV, $5 \times 10^{12} \text{ cm}^{-2}$, 200°C anneal for 5 min	5mm long P-I-N	$\sim 100 \text{ mA/W}$ @ 2-2.5 μm	-	-
Ackert <i>et al.</i> [134]	BDA	B+, 60 keV, 10^{13} cm^{-2} , no anneal	1000x220 nm waveguide, 1mm long APD	0.3 A/W @ 2.02 μm (-30V)	12.5 GHz (1 mm long, -30V)	$< 1 \mu\text{A}$ (-30V)
Hsieh <i>et al.</i> [116]	TPA	waveguide	Waveguide cross-section: width=0.6 μm , heigh=0.5 μm , etch depth=0.22 μm .	1.2 mA/W @ 1310 nm (-15 V) $P_{\text{in}}=208 \mu\text{W}$	-	300 μA (-2 V)
Tanabe <i>et al.</i> [125]	TPA	microdisk resonator	bus waveguide: width=400nm, heigh=220 nm, slab thickness of 60 nm. micro-disk radius= 6 μm	1A/W @ 1537.1 nm (-22 V) $P_{\text{in}}=44.7 \mu\text{W}$	-	$\sim 70 \mu\text{A}$ (-23 V)
Zhu <i>et al.</i> [126]	TPA	lattice-shifted photonic-crystal waveguides	Device length=300 μm slab thickness = 210 nm, lattice constant=400 nm, hole diameter=200 nm.	52 mA/W@1550 nm (-3 V) $P_{\text{in_average}} \sim 7 \text{ mW}$	-	40 pA (-3 V)

Received: ((will be filled in by the editorial staff))

Revised: ((will be filled in by the editorial staff))

Published online: ((will be filled in by the editorial staff))

Keywords: photodetector, infrared, silicon, optical microcavity, graphene.

References

- [1] B. Jalali, and S. Fathpour, *J. Lightwave Technol.* **24**, 4600-4615 (2006).
- [2] M. Paniccia, *Nature Photonics* **4**, 498-499 (2010).
- [3] Y. Kang, P. Mages, A. R. Clawson, P. K. L. Yu, M. Bitter, Z. Pan, A. Pauchard, S. Hummel, and Y. H. Lo, *IEEE Photon. Tech. Lett.* **14**, 1593-1595 (2002).
- [4] A. R. Hawkins, W. Wu, P. Abraham, K. Streubel, J. E. Bowers, *Appl. Phys. Lett.* **70**, 303- 305 (1996).
- [5] Y. Kang, H.-D. Liu, M. Morse, M. J. Paniccia, M. Zadka, S. Litski, G. Sarid, A. Pauchard, Y.-H. Kuo, H.-W. Chen, W. S. Zaoui, J. E. Bowers, A. Beling, D. C. McIntosh, X. Zheng, and J. C. Campbell, *Nature Photonics* **3**, 59-63 (2009).
- [6] P. C. Eng, S. Sung, and B. Ping, *Nanophotonics* **4**, 277-302 (2015).
- [7] J. Michel, J. Liu, L. C. Kimerling, *Nature Photonics* **4**, 527-534 (2010).
- [8] J. Wang, S. Lee, *Sensors* **11**, 696-718 (2011).
- [9] A. W. Poon, S. Feng, Y Li, Y Geng, K.M. Lau, *Proc. of SPIE* **8628**, 86280E-1, (2013).
- [10] M. Casalino, G. Coppola, M. Iodice, I. Rendina, L. Sirleto, *Sensors* **10**, 10571-10600 (2010).
- [11] S. Zhu, H. S. Chu, G. Q. Lo, P. Bai, and D. L. Kwong, *Applied Physics Letters* **100**, 061109 (2012).
- [12] P. Berini, A. Olivieri, C. Chen, *Nanotechnology* **23**, 444011 (2012).
- [13] A. Akbari, R. N. Tait, P. Berini, *Optics Express* **18**, 8505-8514 (2010).
- [14] M. W. Knight, H. Sobhani, P. Nordlander, and N. J. Halas, *Science* **332**, 702–704 (2011).
- [15] A. Sobhani, M. W. Knight, Y. Wang, B. Zheng, N. S. King, L. V. Brown, Z. Fang, P. Nordlander, N. J. Halas, *Nature Communications* **4:1643**, 1-6 (2013).

- [16] M. Amirmazlaghani, F. Raissi, O. Habibpour, J. Vukusic, J. Stake, *IEEE J. of Quant. Elect.* **49**, 589-594 (2013).
- [17] J. J. Ackert, D. J. Thompson, L. Shen, A. C. Peacock, P. E. Jessop, G. T. Reed, G. Z. Mashanovich, A. P. Knights, *Nature Photonics* **9**, 393-7 (2015).
- [18] R. Soref, *Nature Photonics* **4**, 495-497 (2010).
- [19] Y. Zhao, C. Xu, X. Jiang, and H. Ge, *J. Semicond.* **34**, 064009 (2013).
- [20] L. Schares, C. Schow, F. Doany, C. Schuster, J. Kash, D. Kuchta, P. Pepeljugoski, J. Schaub, J. Trehwella, C. Baks, R. John, L. Shan, S. Hegde, Y. Kwark, D. Rogers, F. Libsch, R. Budd, P. Chiniwalla, J. Rosner, C. Tsang, C. Patel, D. Kucharski, D. Guckenberge, R. Dangel, B. Offrein, M. Tan, G. Trott, M. Nystrom, A. Tandon, C. K. Lin, D. Dolfi, *Proc. of 31st European Conference on Optical Communications*, Glasgow, (UK), 3, 369-372 (2005).
- [21] S. V. Kartalopoulos, *IEEE Circuits Devices* **18**, 8-3 (2002).
- [22] C. Decusatis, *Handbook of Fiber Optic Data Communication: A Pratical Guide To Optical Networking* (Elseiver, NJ, USA, 2013), pp. 55.
- [23] R. H. Fowler, *Phys. Rev.* **38**, 45–56 (1931).
- [24] J. Cohen, J. Vilms, R. J. Archer, *Air Force Cambridge Research Labs.* Report No. 68-0651 (1968)
- [25] H. Elabd, W. F. Kosonocky, *RCA Review* **43**, 569-589 (1982).
- [26] R. Stuart, F. Wooten, W. E. Spicer, *Phys. Rev.*, **135**, A495-A505 (1964).
- [27] A. Czernik, H. Palm, W. Cabanski, M. Schulz, U. Suckow, *Appl. Phys. A*, **55**, 180-191 (1992).
- [28] A. Sellai, P. Dawson, *Semicond. Sci. Technol.* **13**, 700-704 (1998).
- [29] C. Scales, P. Berini, *IEEE J. Quantum Electr.* **46**, 633-643 (2010).
- [30] V. E. Vickers, *Applied Optics* **10**, 2190-2192 (1971).

- [31] M. Casalino, *IEEE J. Quantum Electr.*, Accepted.
- [32] S. M. Sze, K. N. Kwok, *Physics of Semiconductor Devices* (Wiley, New York, USA, 2006).
- [33] X. Sang, En-K. Tien, O. Boyraz, *J. Optoelect. and adv. Mat.*, **11**(1), 15-25, (2008).
- [34] N. K. Hon, R. Soref, B. Jalali, *J. of Appl. Phys.*, **110**, 011301 (2011).
- [35] M. Casalino, *Intern. J. Opt. & Appl.*, **2**(1), 1-16 (2012).
- [36] H. K. Tsang, C. S. Wong, T. K. Liang, I. E. Day, S. W. Roberts, A. Harpin, J. Drake, and M. Asghari, *Appl. Phys. Lett.* **80**, 416 (2002).
- [37] M. Dinu, F. Quochi, and H. Garcia, *Appl. Phys. Lett.* **82**, 2954 (2003).
- [38] G. W. Rieger, K. S. Virk, and J. F. Young, *Appl. Phys. Lett.* **84**, 900 (2004).
- [39] H. Yamada, M. Shirane, T. Chu, H. Yokoyama, S. Ishida, and Y. Arakawa, *Jpn. J. Appl. Phys.* **44**, 6541 (2005).
- [40] J. J. Wynne, *Phys. Rev.* **178**, 1295 (1969).
- [41] C. C. Wang and N. W. Ressler, *Phys. Rev. B* **2**, 1827 (1970).
- [42] H. Rong, A. Liu, R. Nicolaescu, M. Paniccia, O. Cohen, and D. Hak, *Appl. Phys. Lett.* **85**, 2196 (2004).
- [43] T. K. Liang and H. K. Tsang, *IEEE J. Sel. Top. Quantum Electron.* **10**, 1149 (2004).
- [44] A. D. Bristow, N. Rotenberg, and H. M. van Driel, *Appl. Phys. Lett.* **90**, 191104 (2007).
- [45] Q. Lin, J. Zhang, G. Piredda, R. W. Boyd, P. M. Fauchet, and G. P. Agrawal, *Appl. Phys. Lett.* **91**, 021111 (2007).
- [46] M. A. Foster and A. L. Gaeta, *Proc. of Conference on Lasers and Electro-Optics/Quantum Electronics and Laser Science - Maryland*, (2007).
- [47] T. G. Euser and W. L. Vos, *J. Appl. Phys.* **97**, 043102 (2005).
- [48] H. Garcia and R. Kalyanaraman, *J. Phys. B* **39**, 2737 (2006).

- [49] O. Boyraz, in *Silicon Photonics for Telecommunications and Biomedicine*, edited by S. Fathpour and B. Jalali (CRC Press, Taylor & Francis Group, 2012)
- [50] W. T. Lotshaw, D. McMorro, and J. S. Melinger, “Measurement of nonlinear absorption and re- fraction in doped si below the band edge,” in *Nonlinear Optics: Materials, Fundamentals and Applications*. Optical Society of America, 2007, p. WE10.
- [51] J. O’Dowd, W.H. Guo, M. Lynch, E. Flood, A.L. Bradley and J.F. Donegan, *Electr. Lett.* **46**(12), 854 – 856, (2010).
- [52] Y. Liu, H. K. Tsang, *Appl. Phys. Lett* **90**, 211105-1-3 (2007).
- [53] M. Fost, J. Niehusmann, T. Plotzing, J. bolten, T. Wahlbrink, C. Moormann, H. Kurz, *Opt. Lett.* **32**, 2046 (2007).
- [54] G. Priem, P. Dumon, W. Bogaerts, D. Van Thourhout, G. Morthier and R. Baets, *Opt. Express* **13**, 9623 (2005).
- [55] I.-W. Hsieh, X. Chen, J. I. Dadap, N. C. Panoiu, R. M. Osgood, S. J. McNab, and Y. A. Vlasov, *Opt. Express* **14**, 12380–12387 (2006).
- [56] R. A. Soref, B. R. Bennett, *IEEE J. Quantum Electron.* **23**, 123 (1987).
- [57] D. F. Logan, P. E. Jessop, and A. P. Knights, *J. Lightwave Technol.* **27**, 930 (2009).
- [58] H. Y. Fan, and A. K. Ramdas, ,” *J. Appl. Phys.* **30**, 1127 (1959).
- [59] L. J. Cheng, J. C. Corelli, J. W. Corbett and G. D. Watkins, *Phys. Rev.* **122**, 761 (1966).
- [60] H. J. Stein, F. L. Vook, J. A. Borders, *Appl. Phys. Lett.* **14**, 328 (1969).
- [61] J. D. B. Bradley, P. E. Jessop, and A. P. Knights, *Appl. Phys. Lett.* **86**, 241103 (2005).
- [62] A. P. Knights, J. D. B. Bradley, S. H. Gou, and P. E. Jessop, *J. Vac. Sci. Technol. A* **24**, 783 (2006).
- [63] P. J. Foster, J. K. Doylend, P. Mascher, and A. P. Knights, *J. Appl. Phys.* **99**, 073101-1 (2006).
- [64] F. L. Vook, H. J. Stein, *Radiation Effects*, **2**, 23 (1969).

- [65] M. W. Geis, S. J. Spector, M. E. Grein, R. T. Schulein, J. U. Yoon, D. M. Lennon, S. Deneault, F. Gan, F. X. Kaertner, and T. M. Lyszczarz, *IEEE Photon. Technol. Lett.* **19**, 152, (2007).
- [66] M. W. Geis, S. J. Spector, M. E. Grein, R. T. Schulein, J. U. Yoon, D. M. Lennon, C. M. Wynn, S. T. Palmacci, F. Gan, F. X. Kärtner, and T. M. Lyszczarz, *Opt. Express*, **15**, 16886 (2007).
- [67] M. W. Geis, S. J. Spector, M. E. Grein, J. U. Yoon, D. M. Lennon, and T. M. Lyszczarz, *Opt. Express*, **17**, 5193 (2009).
- [68] G. Chiarotti, S. nannorone, R. Pastore, and P. Chiaradia, *Phys. Rev. B.* **4**, 3398 (1971).
- [69] T. Baehr-Jones, M. Hochberg, and A. Scherer, *Opt. Express* **16**, 1659 (2008).
- [70] J. J. Ackert, A. S. Karar, J. C. Cartledge, P. E. Jessop, and A. P. Knights, *Opt. Express* **22**, 10710 (2014).
- [71] W. B. Jackson, N. M. Johnson, and D. K. Biegelsen, ,” *Appl. Phys. Lett.* **43**, 195 (1983).
- [72] K. Preston, Y. H. D. Lee, M. Zhang, and M. Lipson, *Opt. Lett.* **36**, 52 (2011).
- [73] J. Esper, P. Panetta, M. Ryschkewitsch, W. Wiscombe, S. Neeck, *Acta Astronautica* **46**, 287-296, (2000).
- [74] C. Daffara, E. Pampaloni, L. Pezzati, M. Barucci, R. Fontana, *Accounts of Chemical Research* **43**, 847 (2010).
- [75] M. Kimata, M. Ueno, H. Yagi, T. Shiraishi, M. Kawai, K. Endo, Y. Kosasayama, T. Sone, T. Ozeki, N. Tsubouchi, *Opto-electronics review* **6**, 1-10 (1998).
- [76] M. Kimata, M. Denda N. Yutani, S. Iwade, N. Tsubouchi, *IEEE J. of Solid-State Circuits* **22**, 1124-1129 (1987).
- [77] M. Casalino, L. Sirleto, L. Moretti, F. Della Corte, I. Rendina, *Journal of Optics A: Pure and Applied Optics* **8**, 909-913 (2006).

- [78] M. Casalino, L. Sirleto, L. Moretti, M. Gioffrè, G. Coppola, M. Iodice, I. Rendina, *Physica E: Low-dimensional Systems and Nanostructures* **41**, 1097–1101 (2009).
- [79] M. Casalino, L. Sirleto, L. Moretti, M. Gioffrè, G. Coppola, I. Rendina, *Appl. Phys. Lett.* **92**, 251104 (2008).
- [80] M. Casalino, G. Coppola, M. Gioffrè, M. Iodice, L. Moretti, I. Rendina, L. Sirleto, *Journal of Lightwave Technology* **28**, 3266 (2010).
- [81] M. Casalino, G. Coppola, M. Iodice, I. Rendina, L. Sirleto, *Optics Express* **20**, 12599-12609, 2012.
- [82] B. Desiatov, I. Goykhman, N. Mazurski, J. Shappir, J. B. Khurgin, U. Levy, *Optica* **2**, 335-338 (2015).
- [83] S. Zhu, M. B. Yu, G. Q. Lo, D. L. Kwong, *Appl. Phys. Lett.* **92**, 081103 (2008).
- [84] S. Zhu, G. Q. Lo, D. L. Kwong, *IEEE Photonics Technology Letters* **20**, 1396–1398 (2008).
- [85] M. Casalino, L. Sirleto, M. Iodice, N. Saffioti, M. Gioffrè, I. Rendina, G. Coppola, *Appl. Phys. Lett.* **96**, 241112 (2010).
- [86] M. Casalino, M. Iodice, L. Sirleto, I. Rendina, G. Coppola, *Optics Express* **21**, 28072-28082 (2013).
- [87] A. R. Zali, M. K. Moravvej-Farshi, *IEEE Journal of Quantum Electronics* **51**, 4000108 (2015).
- [88] M. Hosseinifar, V. Ahmadi, M. Ebnali-Heidari, Iranian Conference on Optics & Photonics & 7th Iranian Conf. on Photonics Engineering, Tehran, 13-15 January (2015).
- [89] Y. P. Huang, L. A. Wang, *Applied Physics Letters* **106**, 191106 (2015).
- [90] S. A. Maier, *Plasmonics: Fundamentals and Applications* (Springer, NY, USA, 2007).
- [91] A. Akbari and P. Berini, *Appl. Phys. Lett.* **95**, 021104 (2009).
- [92] A. Olivieri, A. Akbari, and P. Berini, *Phys. Status Solidi RRL* **4**, 283-285 (2010).

- [93] C. Scales, I. Breukelaar, R. Charbonneau, P. Berini, *J. Lightwave Technol.* **29**, 1852-1860 (2011).
- [94] S. Zhu, G. Q. Lo, D. L. Kwong, *Optics Express* **19**, 15843-15854 (2011).
- [95] M. K. Knight, Y. Wang, A. S. Urban, A. Sobhani, B. Y. Zheng, P. Nordlander, N. J. Halas, *Nanoletters* **13**, 1687-1692 (2013).
- [96] I. Goykhman, B. Desiatov, J. Khurgin, J. Shappir, U. Levy, *Optics Express*, **20**, 28594-28602 (2012).
- [97] I. Goykman, B. Desiatov, J. Khurgin, J. Shappir, U. Levy, *Nano letters* **11**, 2219-2224 (2011).
- [98] R. W. Fathauer, J.M. Iannelli, C. W. Nieh, S. Hashimoto, *Applie Physics Letters* **57**, 1419-1421 (1990).
- [99] R. W Fathauer, S. M. Dejewski, T. George, E. W. Jones, T. N. Krabach, A. Ksendzov, *Applied Physics Letters* **62**, 1774-1776 (1993)
- [100] R. H. Stuart, D. G. Hall, *Applied Physics Letters* **73**, 3815-3817 (1998).
- [101] D. M. Schaadt, B. Feng, E. T. Yu, *Applied Physics Lett.* **86**, 063106 (2005).
- [102] F. Raissi, *IEEE Trans. Electron Devices* **50**, 1134 (2003).
- [103] https://en.wikipedia.org/wiki/Piranha_solution
- [104] M. Fukuda, T. Aihara, K. Yamaguchi, Yu Y. Ling, K. Miyaji, M. Tohyama, *Applied Physics Letters* **96**, 153107 (2010).
- [105] M. A. Nazirzadeh, F. B. Atar, B. B. Turgut, A. K. Okyay, *Scientific Report* **4:7103**, 1-5 (2014).
- [106] K. S. Novoselov, V.I. Fal'ko, L. Colombo, P.R. Gellert, M.G. Schwab and K. Kim, *Nature* **490**, 192-200 (2012).

- [107] J. Dawlaty, S. Shivaraman, J. Strait, P. George, M. Chandrashekar, F. Rana, M. G. Spencer, D. Veksler, Y. Chen, *Appl. Phys. Lett.* **93**, 131905-1–131905-13 (2008).
- [108] B. Sensale-Rodriguez, R. Yan, M. M. Kelly, T. Fang, K. Tahy, W. S. Hwang, D. Jena, L. Liu, H. G. Xing, *Appl. Phys. Lett.* **101**, 26115-126115–3 (2012).
- [109] C.-C. Chen, M. Aykol, C.-C. Chang, A. F. J. Levi, S. B. Cronin, *Nano Letters* **11**, 1863-1867 (2011).
- [110] I. Goykhman, U. Sassi, B. Desiatov, N. Mazurski, S. Milana, D. de Fazio, A. Eiden, J. Khurgin, J. Shappir, U. Levy, A. C. Ferrari, arXiv:1512.08153.
- [111] F. A. Padovani, R. Stratton, *Solid State Electron.* **9**, 69 (1966).
- [112] P. Vabbina, N. Choudhary, A.-A. Chowdhury, R. Sinha, M. Karabiyik, S. Das, W. Choi N. Pala, *ACS Appl. Mater. Interfaces* **7**, 15206-15213 (2015).
- [113] N. Choudhary, J. Park, J. Y. Hwang, W. Choi, *ACS Appl. Mater. Interfaces* **6**, 21215-21222 (2014).
- [114] S. Das, P. Sudhagar, V. Verma, D. Song, E. Ito, S. Y. Lee, Y. S. Kang, W. Choi, *Adv. Funct. Mater.* **21**, 3729-3736 (2011).
- [115] T. K. Liang, H. K. Tsang, I. E. Day, J. Drake, A. P. Knights, and M. Asghari, *Appl. Phys. Lett.* **81**(7), 1323 (2002).
- [116] I.-W. Hsieh, H. Rong, M. Paniccia, Group IV Photonics, 7th IEEE International Conference on, Beijing, (Sep, 2010).
- [117] G. Priem, P. Dumon, W. Bogaerts, D. V. Thourhout, G. Morthier, and R. Baets, *Opt. Express* **13**, 9623 (2005).
- [118] T. J. Johnson, M. Borselli, and O. Painter, *Opt. Express* **14**, 817 (2006).
- [119] M. Soltani, S. Yegnanarayanan, and A. Adibi, *Opt. Express* **15**, 4694 (2007).
- [120] Q. Xu and M. Lipson, *Opt. Express* **15**, 924 (2007).

- [121] Q. Lin, T. J. Johnson, C. P. Michael, and O. Painter, *Opt. Express* **16**, 14801 (2008).
- [122] H. Chen, X. Luo, and A. W. Poon, *Appl. Phys. Lett.* **95**, 171111 (2009).
- [123] J. Bravo-Abad, E. P. Ippen, and M. Soljačić, *Appl. Phys. Lett.* **94**(24), 241103 (2009).
- [124] H. Chen, A. W. Poon, *Appl. Phys. Lett.*, **96**, 191106. (2010)
- [125] T. Tanabe, H. Sumikura, H. Taniyama, A. Shinya, and M. Notimi, *Appl. Phys. Lett.* **96**, 101103 (2010).
- [126] H. Zhu, L. Zhou, R. Yang, X. Li, J. Chen, *Opt. Lett.* **39**(15), 4525-4528, (2014)
- [127] R. Hayakawa, N. Ishikura, H. C. Nguyen, and T. Baba, *Appl. Phys. Lett.* **102**, 031114 (2013);
- [128] Y. Hamachi, S. Kubo, and T. Baba, *Opt. Lett.* **34**(7), 1072–1074 (2009).
- [129] T. Baba, *Nat. Photonics* **2**(8), 465–473 (2008).
- [130] A. Hosseini, X. C. Xu, H. Subbaraman, C. Y. Lin, S. Rahimi, and R. T. Chen, *Opt. Express* **20**(11), 12318–12325 (2012).
- [131] C. Monat, B. Corcoran, D. Pudo, M. Ebnali-heidari, C. Grillet, M. D. Pelusi, D. J. Moss, B. Eggleton, T. P. White, L. O'Faolain, and T. F. Krauss, *IEEE J. Sel. Topics Quantum Electron.*, **16**(1), 344–356, (2010).
- [132] Y. Liu, C. W. Chow, W. Y. Cheung, and H. K. Tsang, *IEEE Photon. Technol. Lett.* **18**, 1882 (2006).
- [133] J. K. Doylend, P. E. Jessop, and A. P. Knights, *Opt. Express* **18**, 13805 (2010).
- [134] J. J. Ackert, D. J. Thompson, L. Shen, A. C. Peacock, P. E. Jessop, G. T. Reed, G. Z. Mashanovich, and A. P. Knights, *Nature Photonics* **9**, 393 (2015).
- [135] X. Mao, P. Han, L. Gao, Y. Mi, S. Hu, Y. Fan, C. Zhao, and Q. Wang, *IEEE Phot. Tech. Lett.* **23**, 1517 (2011).
- [136] S. Park, K. Yamada, T. Tsuchizawa, T. Watanabe, H. Nishi, H. Shinojima, and S. Itabashi, *Opt. Express* **18**, 15303 (2010).

- [137] R. R. Grote, K. Padmaraju, B. Souhan, J. B. Driscoll, K. Bergman, and R. M. Osgood Jr., *Phot. Tech. Lett.*, **25**, 67 (2013).
- [138] D. Korn, H. Yu, D. Hillerkuss, L. Alloatti, C. Mattern, K. Komorowska, W. Bogaerts, R. Baets, J. Van Campenhout, P. Verheyen, J. Wouters, M. Moelants, P. Absil, C. Koos, W. Freude, and J. Leuthold, CLEO 2012, CTu1A.
- [139] B. Souhan, R. R. Grote, J. B. Driscoll, M. Lu, A. Stein, H. Bakhru, and R. M. Osgood Jr., *Opt. Express* **22**, 9150 (2014).
- [140] H. Chen, X. Luo, and A. W. Poon, *Appl. Phys. Lett.* **95**, 171111 (2009).
- [141] H. Zhu, L. Zhou, X. Sun, Y. Zhou, X. Li, and J. Chen, *J. Sel. Top. Quantum Electron.* **20**, 56 (2014).
- [142] D. F. Logan, P. Velha, M. Sorel, R. M. De La Rue, P. E. Jessop, and A. P. Knights, *IEEE Photon. Technol. Lett.* **25**, 67 (2012).
- [143] K. Padmaraju, D. F. Logan, X. Zhu, J. J. Ackert, A. P. Knights, K. Bergman, *Opt. Express* **21**, 14342 (2013).
- [144] K. Padmaraju, D. F. Logan, T. Shiraishi, J. J. Ackert, A. P. Knights, and K. Bergman, *J. Lightwave Tech.* **32**, 505 (2014).
- [145] Q. Li, K. Padmaraju, D. F. Logan, J. J. Ackert, A. P. Knights, and K. Bergman, OFC 2014, paper W3E.5.
- [146] R. Dey, J. K. Doylend, J. J. Ackert, A. Evans, P. E. Jessop and A. P. Knights, *Opt. Express* **21**, 23450 (2013).
- [147] J. K. Doylend, P. E. Jessop, and A. P. Knights, *Opt. Express* **18**, 14671 (2010).
- [148] D. F. Logan, P. Velha, M. Sorel, R. M. De La Rue, A. P. Knights, and P. E. Jessop, *Phot. Tech. Lett.* **22**, 1530 (2010).
- [149] R. Shafiiha, D. Zheng, S. Liao, P. Dong, H. Liang, N. Feng, B. J. Luff, D. Feng, G. Li, J. Cunningham, K. Raj, A. V. Krishnamoorthy, and M. Asghari, OFC 2010,

OMI8.

- [150] D. F. Logan, K. J. Murray, J. J. Ackert, P. Velha, M. Sorel, R. M. De La Rue, P. E. Jessop, and A. P. Knights, *J. of Opt.*, **13**, 125503 (2011).
- [151] J. J. Ackert, M. Fiorentino, D. F. Logan, R. G. Beausoleil, P. E. Jessop, A. P. Knights, *J. of Nanophot.* **5-1**, 059507 (2011).
- [152] S. T. Fard, K. Murray, M. Caverley, V. Donzella, J. Flueckiger, S. M. Grist, E. Huante-Ceron, S. A. Schmidt, E. Kwok, N. A. F. Jaeger, A. P. Knights, and L. Chrostowski, *Opt. Express* **22**, 28517 (2014).
- [153] J. J. Ackert, A. P. Knights, M. Fiorentino, R. Beausoleil, P. E. Jessop, “Defect Enhanced Silicon-On-Insulator Microdisk Photodetector,” Optical Interconnects Conference, 2012, 76, TuP10.
- [154] L. Haret, X. Checoury, Z. Han, P. Boucaud, S. Combrie, and A. De Rossi, *Opt. Express* **18**, 23965 (2010).
- [155] R. R. Grote, J. B. Driscoll, N. C. Panoiu, and R. M. Osgood Jr., IPR 2012, Colorado Springs, June 2012, IW3C.6.
- [156] K. K. Mehta, J. S. Orcutt, O. Tehar-Zahav, Z. Sternberg, R. Bafrali, R. Meade, and R. J. Ram, *Scientific Reports* **4**, 4077 (2014).
- [157] J. J. Ackert, A. S. Karar, D. J. Paez, P. E. Jessop, J. C. Cartledge, and A. P. Knights, *Opt. Express* **21**, 19530 (2013).
- [158] R. A. Soref, *Nature Photonics* **4**, 495 (2010).
- [159] W. M. Green, B. Kuyken, Z. Liu, M. A. Van Camp, S. Assefa, D. M. Gill, T. Barwicz, S. M. Shank, Y. A. Vlasov, R. M. Osgood, Jr., R. Baets, G. Roelkens, OFC 2013, OTh4I.7
- [160] G. Roelkens, U. Dave, A. Gassenq, N. Hattasan, C. Hu, B. Kuyken, F. Leo, A. Malik, M. Muneeb, E. Ryckeboer, Z. Hens, R. Baets, Y. Shimura, F. Gencarelli, B. Vincent,

- R. Loo, J. Van Campenhout, L. Cerutti, J. B. Rodriguez, E. Tournie, X. Chen, M. Nedeljkovic, G. Z. Mashanovich, L. Shen, N. Healy, A. C. Peacock, X. Liu, R. Osgood, and W. J. Green, *IEEE J. Sel. Top. Quantum Electron.* **20**, 8201511 (2014).
- [161] B. Souhan, C. P. Chen, R. R. Grote, J. B. Driscoll, N. Ophir, K. Bergman, and R. M. Osgood Jr., *Phot. Tech. Lett.* **25**, 2031 (2013).
- [162] B. Souhan, R. R. Grote, C. P. Chen, H. Huang, J. B. Driscoll, M. Lu, A. Stein, H. Bakhru, K. Bergman, W. M. J. Green, and R. M. Osgood Jr., *Opt. Express* **22**, 27415 (2014).
- [163] D. J. Thompson, L. Shen, J. J. Ackert, E. Huante-Ceron, A. P. Knights, M. Nedeljkovic, A. C. Peacock, and G. Z. Mashanovich, *Opt. Express* **22**, 10825 (2014).

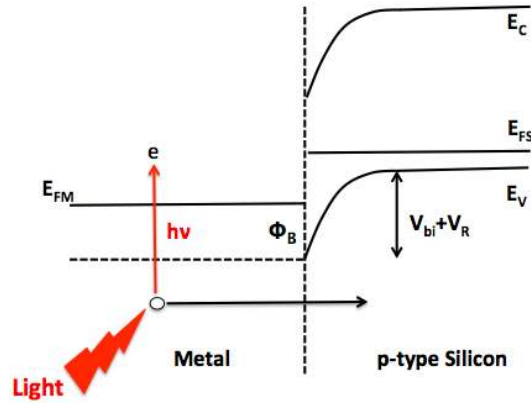


Figure 1. Energy band diagram for a metal/p-type Si junction (E_{FM} and E_{FSi} are the metal and Si Fermi level. E_C and E_V are the conduction and valence band energy of Si. V_{bi} and V_R are the built-in potential and external reverse bias applied, respectively).

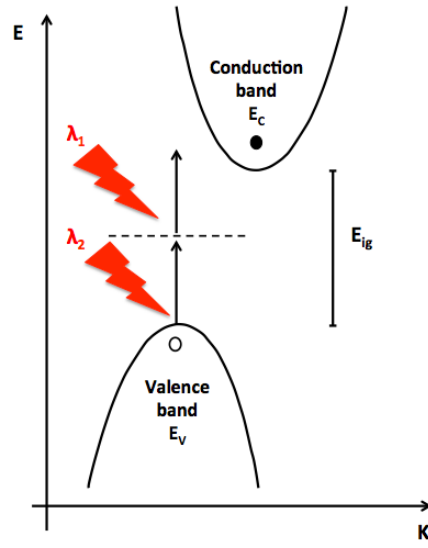


Figure 2. Band diagram of the two-photon absorption mechanism.

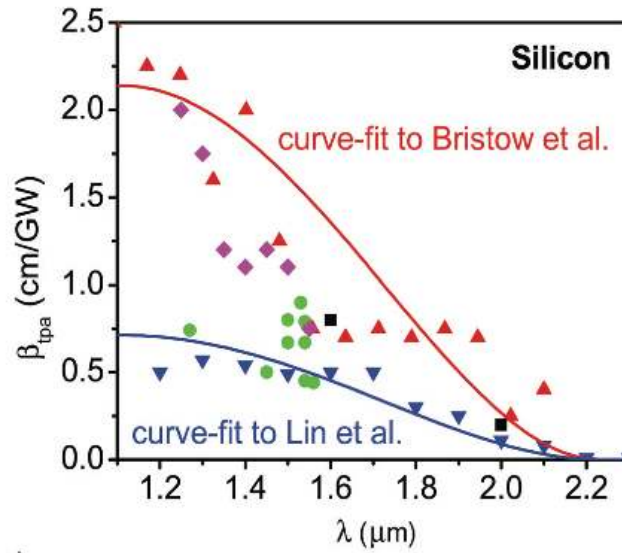


Figure 3. Experimental β of Si as function of wavelength collected by Hon *et al.* [34]. Data points are determined from Refs. [36-43] (circles), Ref. [44] (upward triangles), Ref. [45] (downward triangles), Ref. [46] (diamonds), and Ref. [47] (squares). One theoretical dispersion curve is fitted to Ref. [44] (Bristow *et al.*) and another to Ref. [45] (Lin *et al.*).

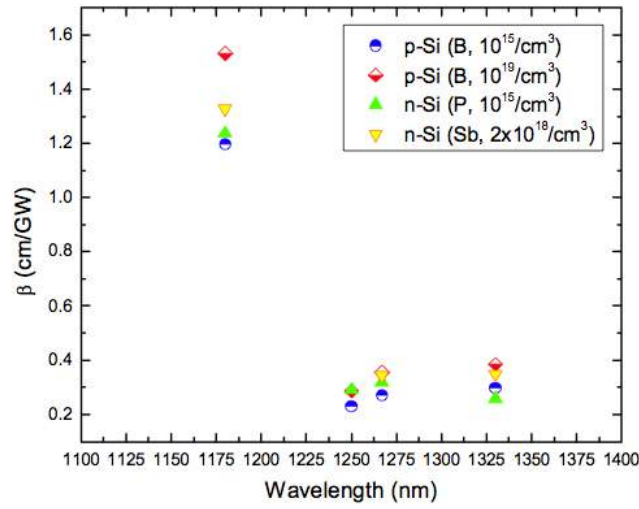
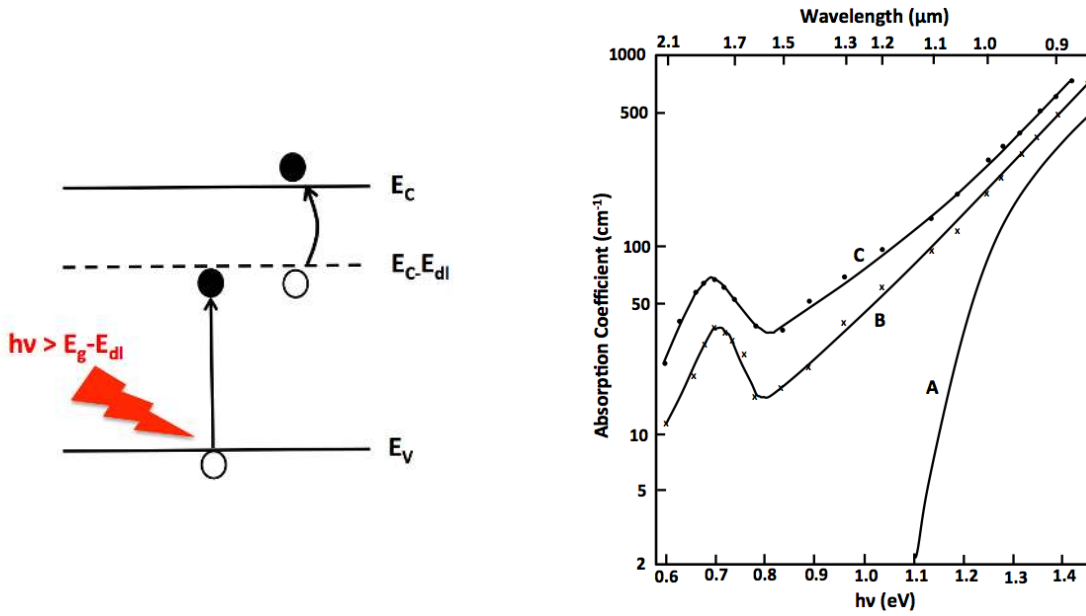
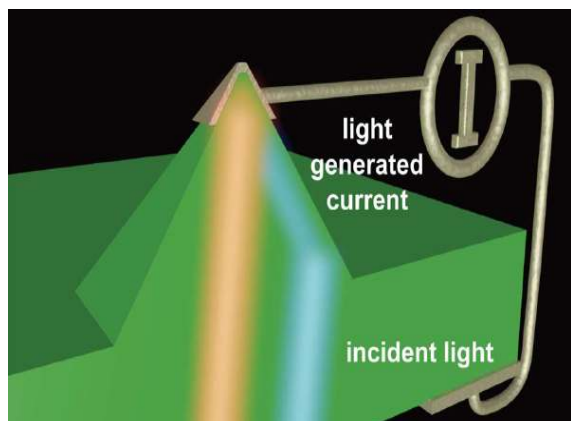


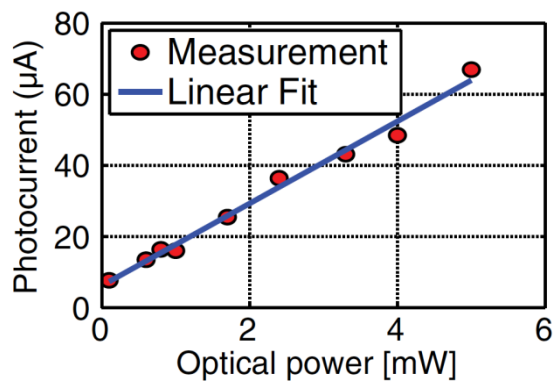
Figure 4. β as a function of laser wavelength for various doping concentrations in silicon [50].



(a) (b)
Figure 5. (a) Energy level diagram showing the conduction band energy E_c , valence band energy E_v , bandgap energy $E_g=E_c-E_v$ and deep level located E_{dl} below the conduction band. A photon of energy $h\nu$ provides optical excitation of electron from valence band into the deep level state, and the carrier is subsequently thermally excited into the conduction band. (b) Absorption spectrum of pure silicon (A) and deuteron irradiated silicon (B and C) [58].



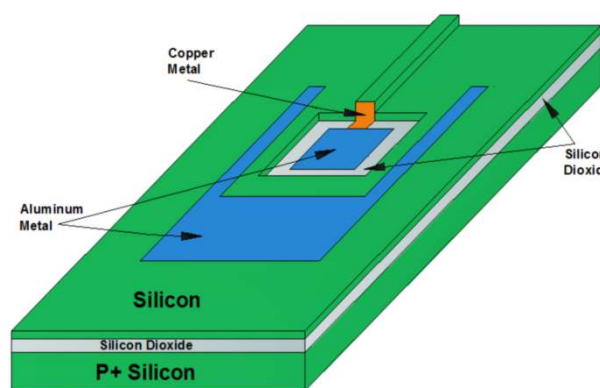
(a)



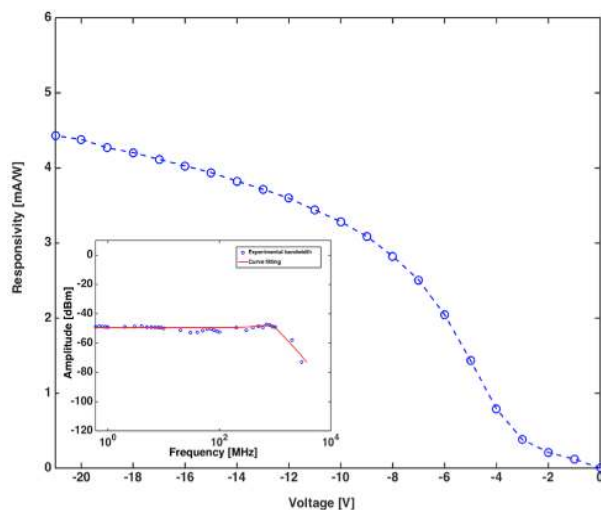
(b)

Figure 6. (a) Schematic representation of the pyramidally shaped PDs reported in Ref. [82].

(b) Photocurrent versus optical power data and linear fit for 1550 nm wavelength.



(a)



(b)

Figure 7. (a) Schematic representation of the PD proposed in Ref. [86]. Responsivity versus

reverse voltage applied. (b) Responsivity vs. reverse voltage and experimental PD bandwidth

(inset).

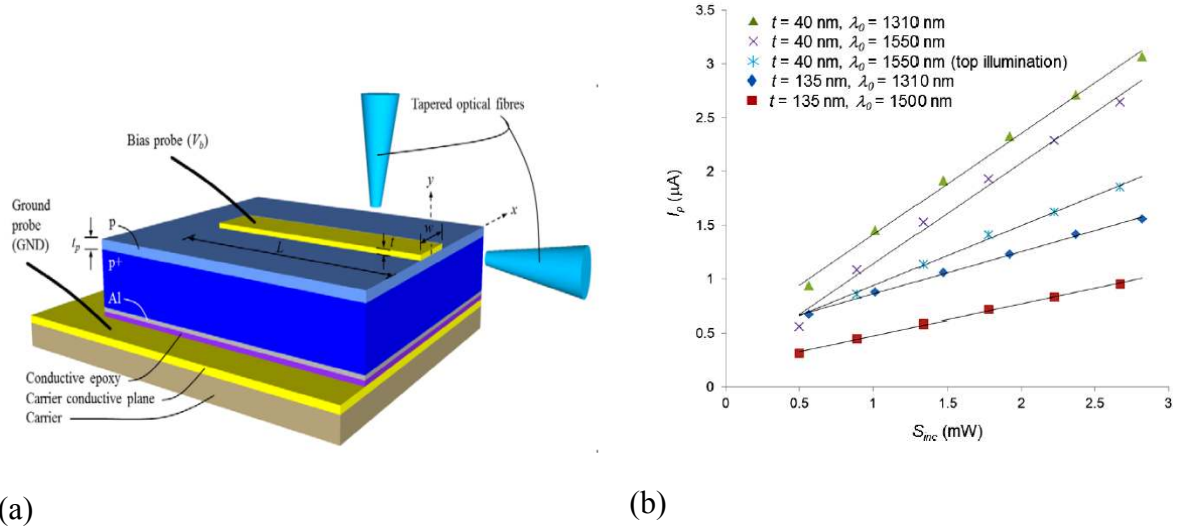


Figure 8. (a) Sketch of the Au Schottky surface plasmon PD on p-Si proposed in Ref. [12, 13]. The Au stripe of width w , thickness t and length L supports SPPs. (b) Measured photocurrent (I_p) versus incident optical power (S_{inc}) for different geometry, wavelengths and illumination type.

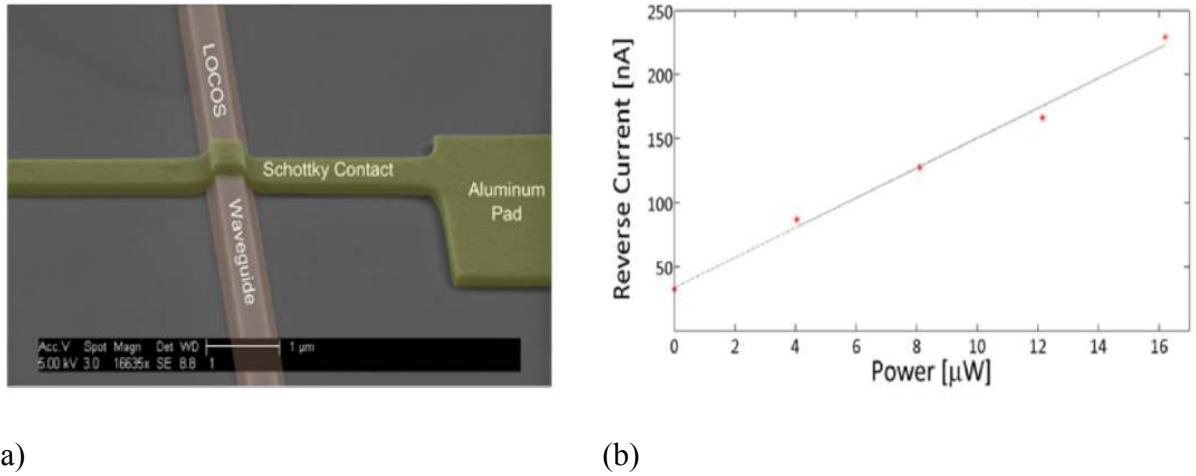
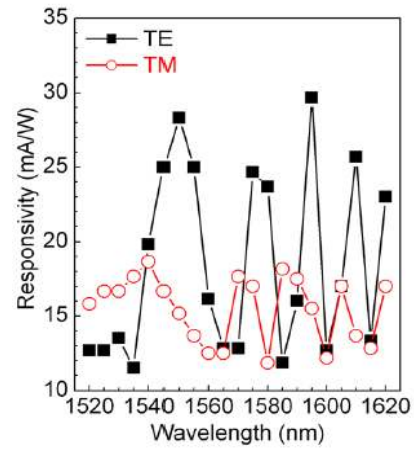
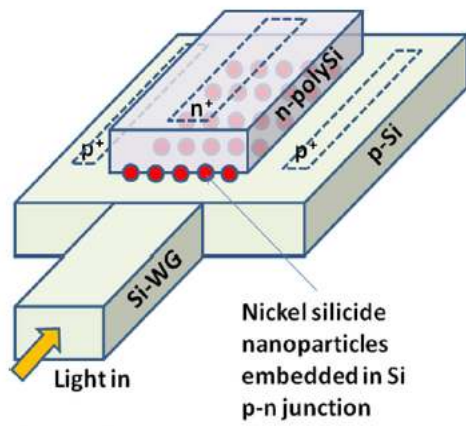


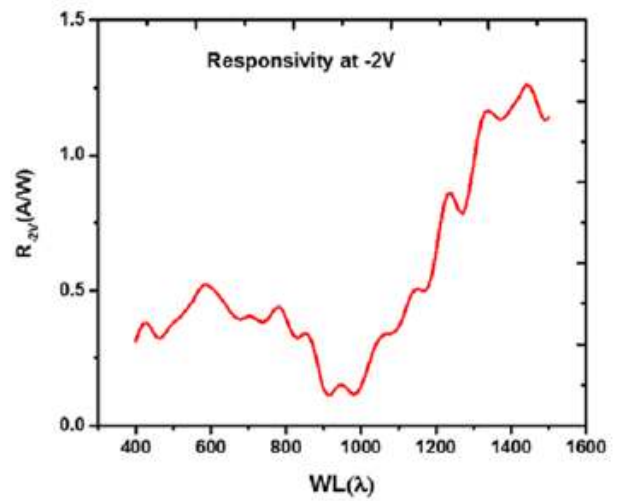
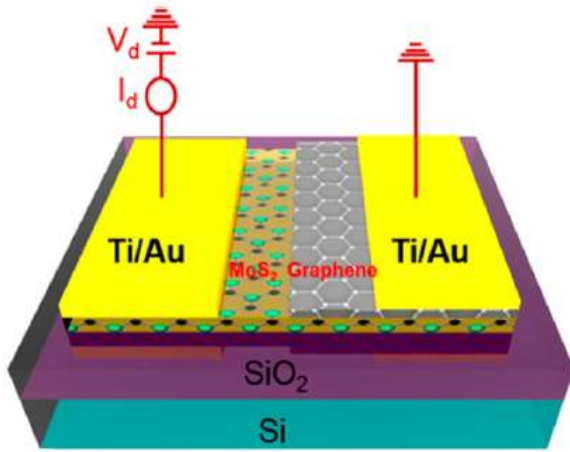
Figure 9. (a) SEM micrograph of the locally-oxidized silicon bus waveguide integrated with the Schottky PD reported in Ref. [96]. (b) The responsivity plot of the device at 1550 nm. The reverse current is taken at -0.1 V of reverse bias.



(a)

(b)

Figure 10. (a) Schematic of the Si waveguide-integrated PD based on the embedded metal silicide NPs proposed in Ref. [11]. (b) Responsivity at -5 V for quasi-TE and quasi-TM lights.



(a)

(b)

Figure 11. (a) MoS₂/graphene Schottky PD proposed in Ref. [112]. (b) Responsivity at different wavelengths (spectral response).

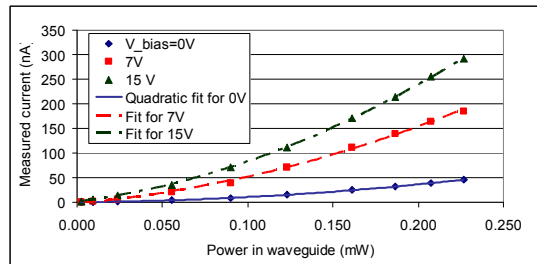
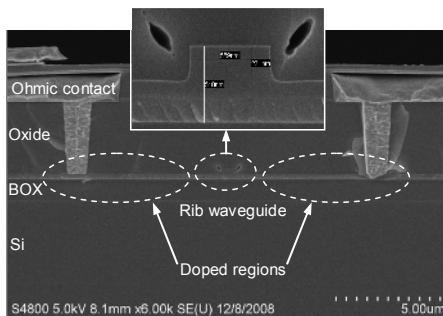


Figure 12. (a) SEM image of the structure fabricated at Intel Corporation by Hsieh *et al.*

[116]. (b) TPA- induced current as a function of optical power inside the waveguide for various reverse-bias conditions.

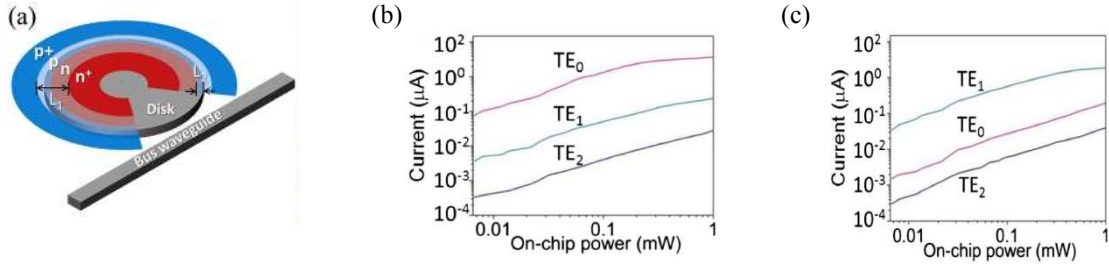


Figure 13. Sketch of the devices studied by Zhu *et al.* [126]. (a) TPA-induced current by three transverse electric whispering gallery modes (TE₀, TE₁, and TE₂) as a function of optical power for device I (b) and II (c).

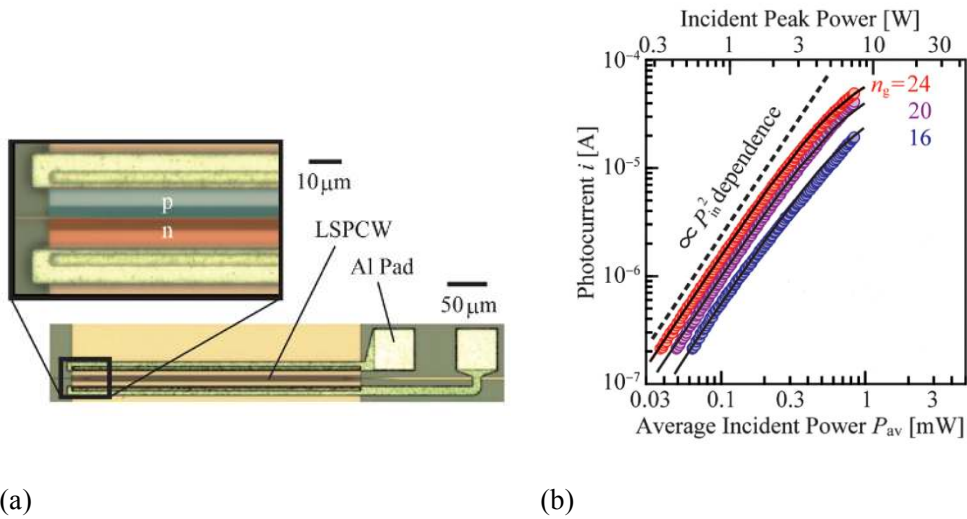


Figure 14. (a) LSPCWs-based device from Baba's group [127]. (b) TPA-induced current as function of the average powers from sub- μ W to sub- mW (or peak powers from sub-10 mW to sub-10 W) for three different group indexes. Circular plots and solid lines are experimental and theoretical results, respectively.

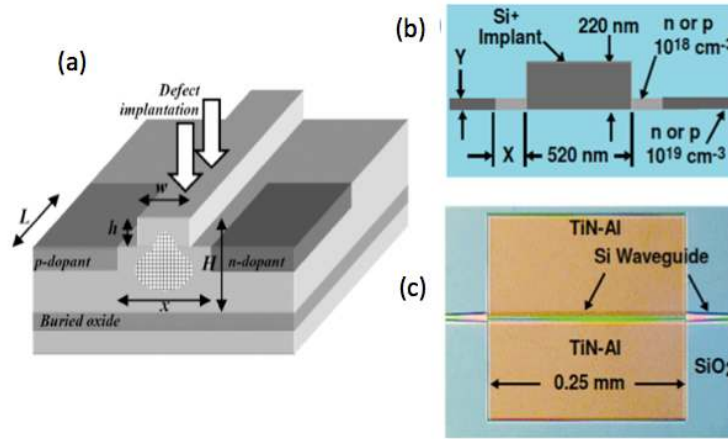


Figure 15. In-line defect-mediated photodiode structures: (a) Cross-section of a lateral P-I-N diode on a large ridge waveguide, of the type used in early demonstrations [61, 62, 132], (figure from Ref. [57]). (b) cross-section (top) and top view (bottom) of device used first by Geis *et al.* [67] and in many recent demonstrations [65, 136, 137, 162] (figure from Ref. [67]).

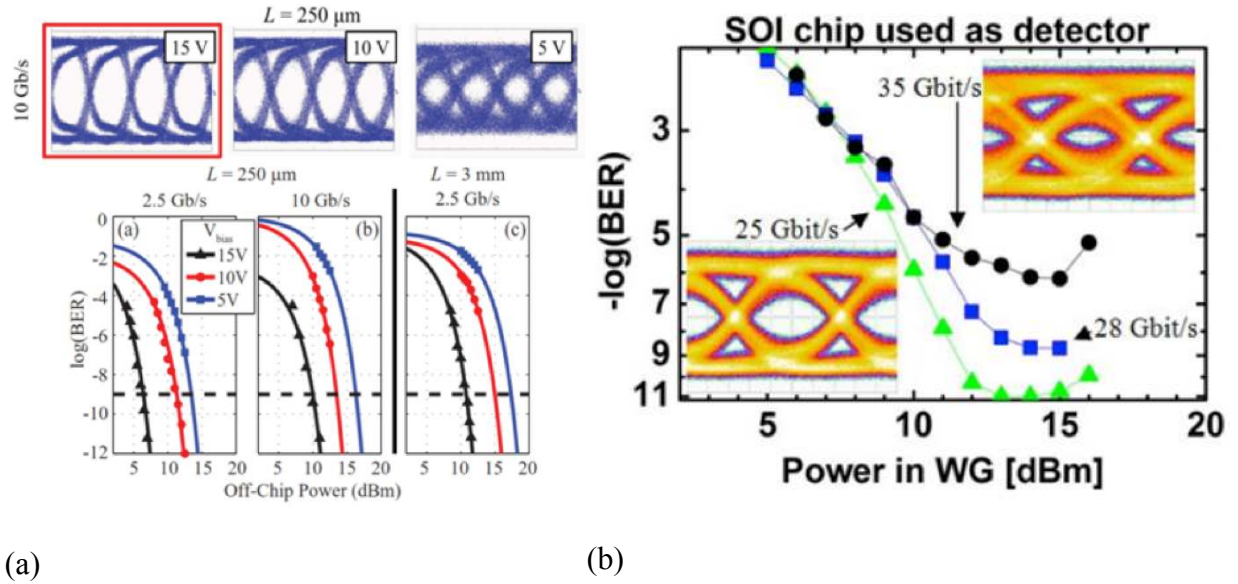


Figure 16. (a) 10 Gb/s eye diagrams at different applied bias for 0.25 mm long P-I-N and waterfall curves for varied bias, bitrate, and P-I-N length [137]. (b) Eye diagrams and waterfall curves of 3 mm long P-I-N at varied bitrate [138].

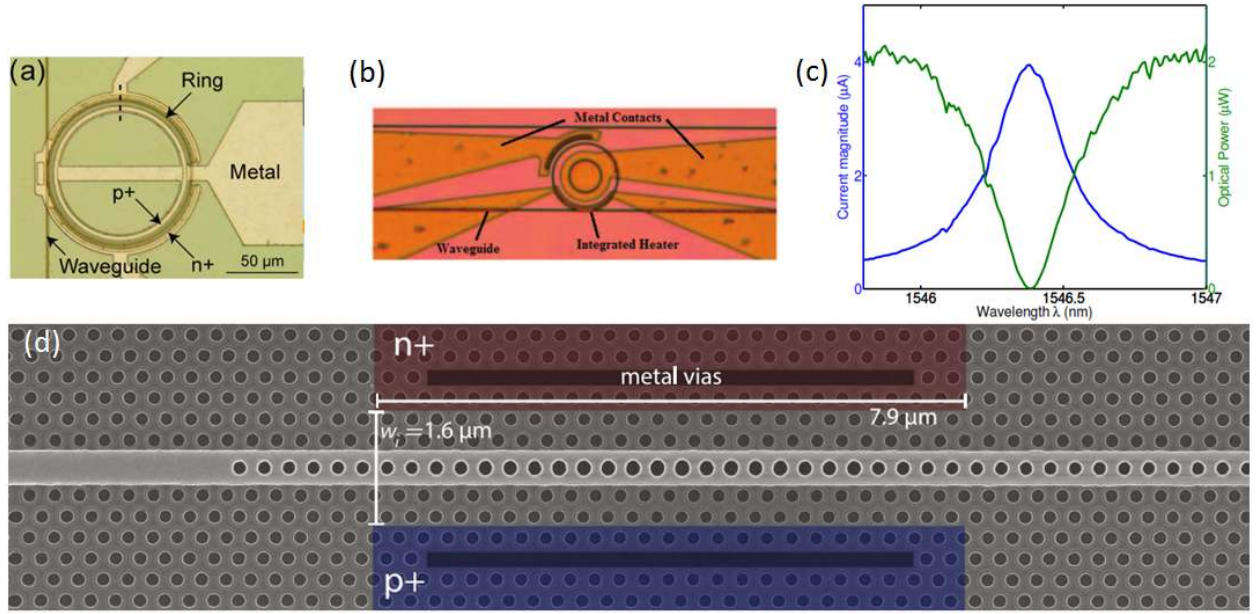


Figure 17. (a) Ring-resonator photodiode formed of polysilicon demonstrated by Preston *et al.* [72]. (b) Ion-implanted ring resonator demonstrated with integrated heater for resonance tuning by Ackert *et al.* [151]. (c) Typical photocurrent response and optical transmission from ring resonator photodiode from Fard *et al.* [152]. (d) Photonic crystal cavity photodiode demonstrated by Mehta et al [156].

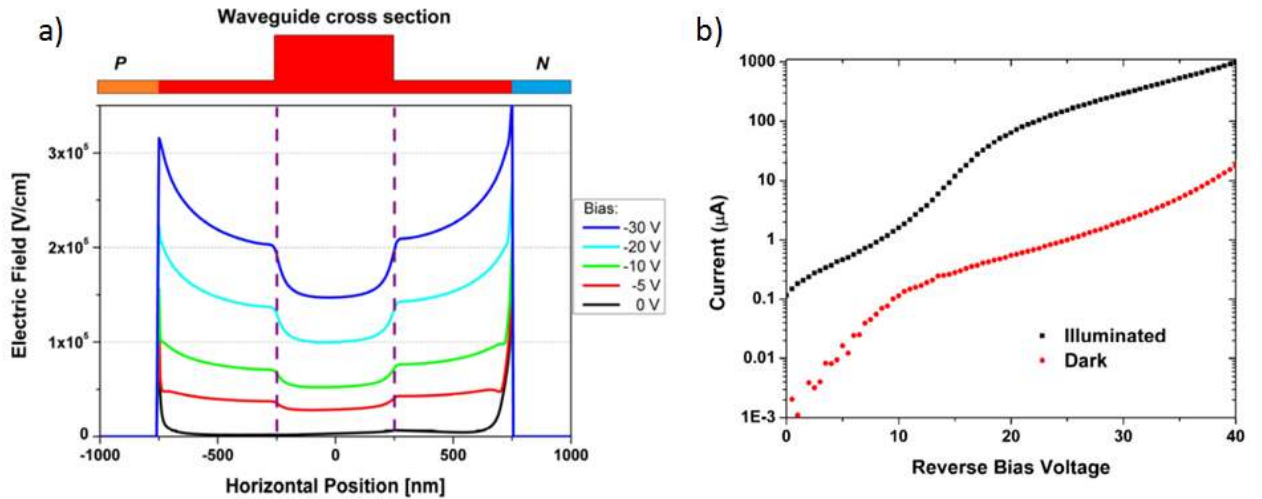


Figure 18. (a) Cross-section of the defect-mediated APD structure and electric field distribution simulation. (b) IV characteristic under dark and illuminated conditions [157].

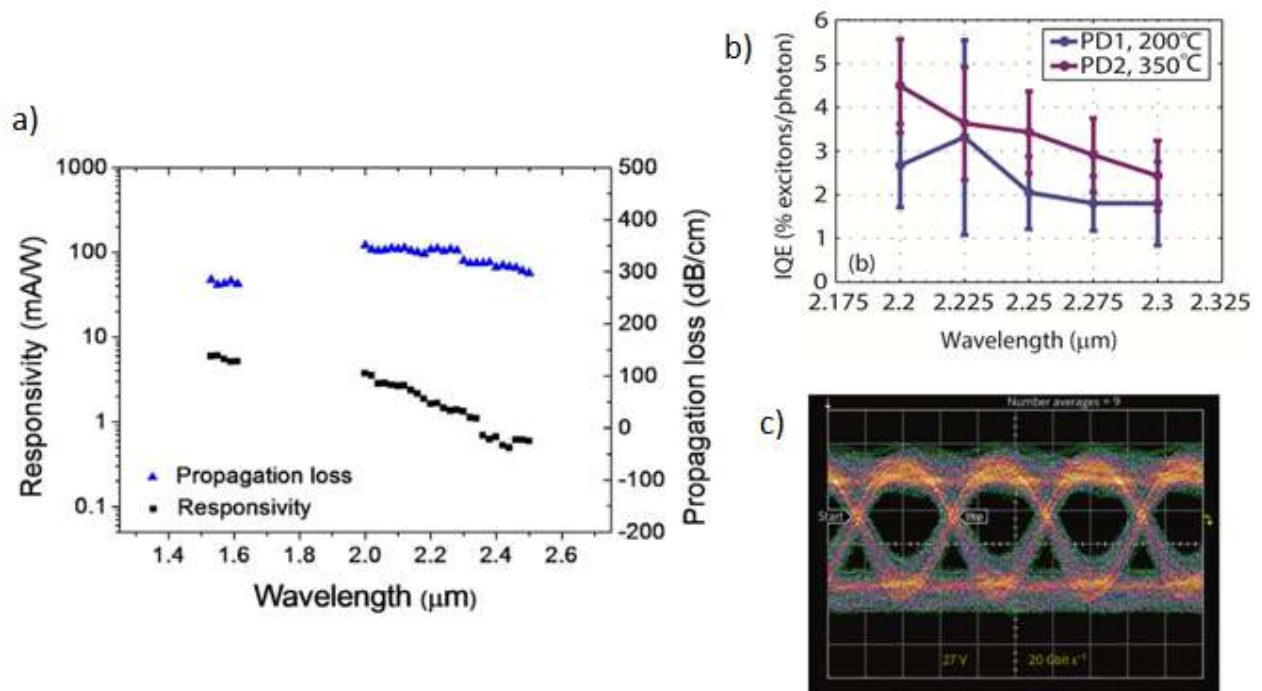


Figure 19. (a) Responsivity and propagation loss of device in Ref. [163], at C-band and 2-2.5 μm wavelengths. (b) Extracted internal quantum efficiency of device in Ref. [162] at 2.2-2.3 μm wavelengths. (c) 20 Gb/s eye diagram from APD operating at 1.96 μm wavelength [134].



Maurizio Casalino graduated *summa cum laude* in Electronic Engineering at University of Naples "Federico II" in 2003. In 2008 he received the Ph.D. degree in Engineering Electronic at University "Mediterranea" of Reggio Calabria and in the same year he joined as researcher to the Institute for Microelectronics and Microsystems of the Italian National Council of Research. Currently he is responsible of the course of Physics of the Semiconductors and Devices at University of Caserta (Italy).



Giuseppe Coppola received the Electronic Engineering degree and Ph.D. degrees from University of Naples "Federico II", in 1997 and 2001, respectively. Currently, he is a senior researcher at Institute for Microelectronics and Microsystems. Since 2004, he has been leader of the optoelectronic Lab of that institute. His main research interests concern the design fabrication and characterization of silicon-based optoelectronics devices, and the non-contact optical characterization techniques.



Richard De La Rue retired from the University of Glasgow in September 2010 and joined the Photonics Research Centre at the University of Malaya in April 2011. In August 2012 he took became Research Professor of Optoelectronics in the School of Engineering at the University of Glasgow - and completed his tenure in July 2014. He is Fellow of the European Optical Society; Fellow of the IEEE; Fellow of the OSA; Fellow of the Royal Academy of Engineering; Fellow of the Royal Society of Edinburgh and Fellow of the Institution of Engineering and Technology. His Hirsch index, according to Google Scholar, is 52.



Dylan Logan received his B. Eng. and Ph. D. from McMaster University in 2007 and 2011, respectively, in the Department of Engineering Physics. Between 2011 and 2013, he was a postdoctoral fellow in the Department of Electrical and Computer Engineering at the University of Toronto. He is currently a designer with the silicon photonics team at Ranovus, located in Ottawa, Ontario, Canada.

Graphical Abstract

This review focuses on sub-bandgap all-silicon photodetectors operating at telecom and datacom wavelengths. After a short introduction to the theory of the main photo-conversion mechanisms allowing detection at sub-bandgap wavelengths in silicon, an overview of the more recent all-silicon photodetectors based on both innovative structures and emerging materials, will be presented, discussed and compared. The review also helps identifying future developments necessary to compare favourably with devices based on III-V elements.

